Development of a Helicon Plasma Receiver for Wireless Power Transfer

John Correy

A thesis

submitted in partial fulfillment of the

requirements for the degree of

Master of Science in Aeronautics and Astronautics

University of Washington

2021

Committee:

Uri Shumlak

Carl Knowlen

Program Authorized to Offer Degree:

Aeronautics and Astronautics

University of Washington

Abstract

Development of a Helicon Plasma Receiver for Wireless Power Transfer

John Correy

Chair of the Supervisory Committee:

Uri Shumlak

Aeronautics and Astronautics

Typical research of long distance wireless power transfer systems is limited to electromagnetic waves, specifically microwave and laser systems. Plasma provides an appealing alternative due to its internal charge separation and current, as well as its potential for direction via magnetic field. To investigate this, a helicon plasma source at the University of Washington is used in conjunction with a modified Langmuir probe, which consists of two large separated electrodes. Plasma is fired at the electrodes, seeking to drive power over a resistive load. Measurements show a peak average power of 0.35 W in this experimental configuration. Improvements in electrode geometry are explored via electric field calculation and particle simulations. Results suggest that the technology is potentially viable with further optimization.

Contents

List of Figures

List of Tables

List of Abbreviations

WPT	**W**ireless **P**ower **T**ransmission (or Wireless Power Transfer)
EM	**E**lectro**m**agnetic wave
HPH	**H**igh **P**ower **H**elicon
APL	**A**dvanced **P**ropulsion **L**aboratory
RF	**R**adio **F**requency
VASIMR	**Va**riable **S**pecific **I**mpulse **M**agnetoplasma **R**ocket
RC	**R**esistor-**C**apacitor circuit
RLC	**R**esistor-**I**nductor-**C**apacitor circuit
TRL	**T**echnology **R**eadiness **L**evel
IV	**c**urrent-**v**oltage curve
PPT	**P**ulsed **P**lasma **T**hruster

List of Symbols

a	bounded wave radius	m
B	magnetic field	T
c	speed of light	$2.99792458 \times 10^{8}\ \mathrm{m\,s^{-1}}$
e	elementary charge	$1.602176634 \times 10^{-19}\ \mathrm{C}$
E	electric field	$\mathrm{V\,m^{-1}}$
j	current density	$\mathrm{A m^{-2}}$
k	vector wave-number	
k	Boltzmann constant	$1.380649 \times 10^{-23}\ \mathrm{J\,K^{-1}}$
m	wave mode	
n	number density	$\mathrm{m^{-3}}$
p	pressure	Torr
P	power	W
R	resistance	Ω
t	time	s
T	temperature	eV or K
V	voltage	V
β	ratio of thermal and magnetic pressure	
ε	permittivity	$\mathrm{F\,m^{-1}}$
θ	angle	rad
λ_{mfp}	mean free path	m
μ_0	vacuum permeability	$1.25663706212 \times 10^{-6}\ \mathrm{H\,m^{-1}}$
ρ	free charge density	$\mathrm{C m^{-3}}$
σ	ionization cross section $\mathrm{m^2}$	
φ	voltage (scalar function)	V
ω	angular frequency	$\mathrm{rad\,s^{-1}}$

Acknowledgements

Foremost thanks must go to Professor Robert Winglee. In addition to being the project's principal investigator he was an amazing advisor, professor, and role model. It's safe to say I wouldn't have gotten here without his guidance. He is sorely missed.

I'd also like to thank Professors Uri Shumlak, Carl Knowlen, and Michael McCarthy, who were each critical in helping me finish this work (and put up with my last minute questions).

Navigating grad school would have been impossible without the support of my colleagues Keon Vereen, Paige Northway, Manolo Azuara, Paul Sturmer, and Mariah Danner. I couldn't have asked for better mentors.

This work never would have happened without the assistance of my undergraduate teammates. Kyle McEleney, Sohra Ma, Caroline Paxton, Jade Cutter, Marshall Lee, and Grace Zoppi were all critical in getting the experiment up and running and assisting with testing. I wish them all the best of luck in their future endeavors.

I'm also grateful for the support of the Aeronautics and Astronautics Department and the Earth and Space Sciences Department for their academic and laboratory support. I'd also like to thank the Washington NASA Space Grant Consortium for their financial and career support.

Finally, I have to thank my family and friends for forcing me to take breaks throughout this whole process. It's been a stressful year and they've been great at keeping me sane.

Chapter 1

Introduction

1.1 Purpose of System

With goals of a significant, extended human presence in space becoming much more attainable, the infrastructure surrounding exploration has faced increasing challenges. The environments and conditions human explorers will face require more complex and creative solutions than early landers and rovers. Whether fulfilling physical, psychological, or mission based needs, human exploration will require a massive overhaul of conventional space infrastructure. This work does not seek to solve all of these problems, but will focus on a new method of transferring power between critical mission infrastructure.

This research does not seek to reinvent standardized power distribution, such as cabling and transformers, but instead seeks to explore a new possibility for more flexible uses. Long distance, temporary, and otherwise uncommon transmission needs are typically proposed to be solved with Wireless Power Transmission (WPT) systems. Most WPT proposals focus on the use of microwave or laser power beaming systems, as they are proven technologies. The plasma system in this work operates in a similar configuration, but seeks to solve (or bypass entirely) several shortcomings of microwave and laser transmission.

1.2 System Context and History

The concept of transmitting power wirelessly is not a novel one. The ability to manipulate electrons remotely has been known since the discovery of Ampere's Law in the 1830s, though the means of accomplishing it were still unknown. In the 1880s, however, Hertz was able to confirm the existence of the theoretical electromagnetic wave, paving the way for its future use in a variety of technologies [1]. In the nearly century and a half since that discovery, the use of electromagnetic waves has changed nearly every facet of human life, from technological developments like RADAR and cell phones to commercial uses, such as microwave ovens and tanning salons. But it is only in recent decades that electromagnetic waves as a means of transmitting power has received any significant adoption. In 1988 a team at the University of Toronto powered a model aircraft using microwaves, allowing it to fly at an altitude of 150 meters for 20 minutes [2]. Similarly, solar panels have begun to see widespread use, allowing people to draw power from visible light.

These technologies have proved that wireless power transfer over a distance is possible, but work to transmit a considerable amount of power over a great distance is ongoing. This section seeks to review the state of existing WPT technology, as well as provide justification for the decision to use a plasma-based system to solve the same problems.

1.2.1 Established Means of Wireless Power Transmission

Earth-based means of wireless power transmission have seen widespread, though application limited, use. For very short range systems this technology can be simple and efficient; just look to the growing usage of charging pads for cell phones and smart devices. But transmitting power over greater distances is far more difficult. In these cases the simpler means, like inductive charging, simply cannot cover the distance needed to be useful. Instead researchers focus on radiative techniques. Notably, harnessing electromagnetic (EM) waves in the microwave and visible light ranges.

Microwave power transmission has already seen real-world implementation. Grand Bassin, on Réunion Island, uses a microwave WPT system to transmit power from the station to tourist lodges 700 meters away without disturbing the natural environment [3]. To do this, a set of 60 magnetrons sends power to an array of cyclotron wave converters and rectennas. In total, the system transmits around 10 kW of power at an estimated 20% efficiency. The layout of the system can be seen in Fig. 1.1.

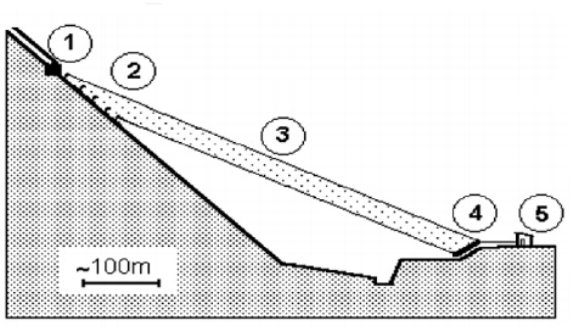

1. Water pumps / Grid power
2. Beam Projector Array
3. Microwave Beam
4. Receiving CVC / Rectenna Array
5. End Users

FIGURE 1.1: The layout of the WPT system in Grand Bassin [3]

Most microwave WPT systems follow the same approach as the Grand Bassin system. A microwave is generated and radiates until it reaches a receiving antenna, which transforms it to usable power through rectifiers [4]. The individual components can vary; magnetrons are well-established, but alternatives like helical antennas are under investigation as well [5]. Even in cutting-edge research, however, efficiency drops off significantly as distance increases. Recent publications show that the technology works over larger distances, but shows total system efficiency on the order of 1 or 2% for distances of around 10 km [4]. Microwave WPT systems are promising, but significant development is needed before they will be truly feasible for widespread use.

The other commonly studied means of WPT is the use of laser systems. In these cases a laser is generated and directed to charge a photovoltaic cell. As with the microwave system, laser WPT has been proven on Earth in a variety of ways, including the flight of a model aircraft [6]. Though large-scale systems, like the Grand Bassin system, have not yet been implemented, performance predictions are possible from testing. Photovoltaic cells are typically estimated at 40 - 50% efficiency, and testing has estimated overall efficiency to be on the order of 10% under ideal conditions [7]. In non-ideal conditions, whether these be from external effects like scattering or experimental effects, this efficiency quickly drops.

In both practice and proposed implementation, microwave and laser WPT systems fill similar, if not identical, niches. A key area that both technologies have been proposed for is WPT in space systems. A commonly discussed use is transmitting power between a satellite and the body it is orbiting. There are different variants of this - power beaming has been proposed as a solution to the energy crisis, where large orbiting solar farms would transmit power back down to Earth [8]. Others propose sending power up from a body to an orbiting spacecraft in order to charge it and reduce the mass allocated to batteries [9]. But each of these cases run into similar issues - beam dispersion, line-of-site limitations, and generally low efficiency. The introduction of a new technology is needed to push progress forward.

1.2.2 History of the Helicon Experiment

The generation of a consistent, long range plasma beam requires significantly different technology than the generation of an EM wave. The design of a directed plasma stream is nothing new though; it comes about as a natural result of other technologies. As such, the mechanisms used in this work are derived from, and therefore require an understanding of, electric propulsion concepts. For the system developed here, an established High Power Helicon (HPH) source was used for plasma generation as it has significant history at UW and can generate a well collimated, properly layered plasma stream.

Development and study of a helicon plasma source has been conducted at the University of Washington Advanced Propulsion Lab (APL) for nearly two decades, with early work being intended to create a seed plasma that could fill a magnetic field [10]. These simulations led to the development of a helicon system that was simple to implement and could be adapted to serve many research purposes. At their most basic, helicon sources consist of a helical antenna aligned with an axial magnetic field. When particles enter the antenna they are coupled to an RF wave, and a plasma is formed. The material that will become the plasma can vary greatly. While some investigation has showed that a helicon antenna can be used to improve performance of another thruster [11], most systems use gas injection. This plasma is then forced out of one (or both) ends of the source region. The layout of this can be seen in Fig. 1.2.

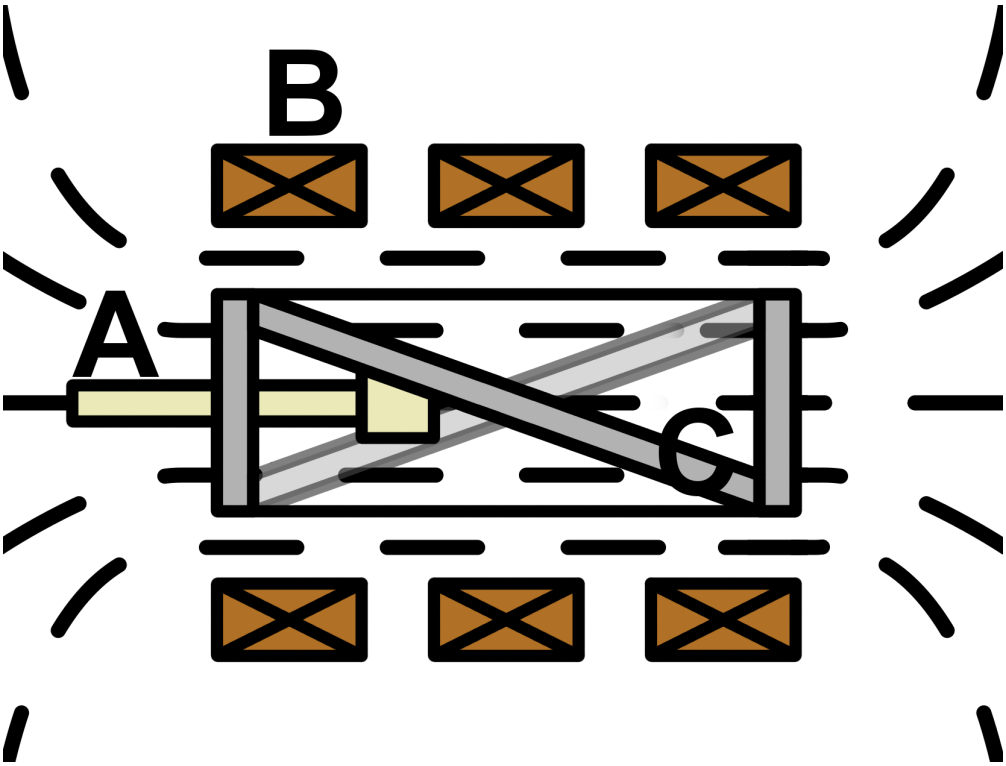

FIGURE 1.2: A basic helicon source, with gas injection (A), base magnetic field (B) and a right-hand antenna (C)

Since then, research into helicon systems at the UW has expanded greatly. In 2008 the aforementioned simulations were verified experimentally, with downstream magnetic field and current

properties measured in the group's first High Power Helicon system [12]. Around the same time, simulated work showed that the inclusion of a magnetic nozzle could greatly increase downstream density and uniformity, allowing beams to propagate hundreds or thousands of meters [13]. This configuration can be seen in Fig. 1.3. This work was soon verified experimentally as well, and proved to be a guiding discovery for helicon work at the university [14]. The focusing effect of the downstream nozzle, combined with growing interest in the RF coupling involved in plasma generation, led to breakthroughs in clustering effects of multiple helicon thrusters. This was first investigated by Murakami, [15], and improved upon and characterized by Vereen by 2019 [16]. A helicon system firing in a high power mode can be seen in Fig. 1.4.

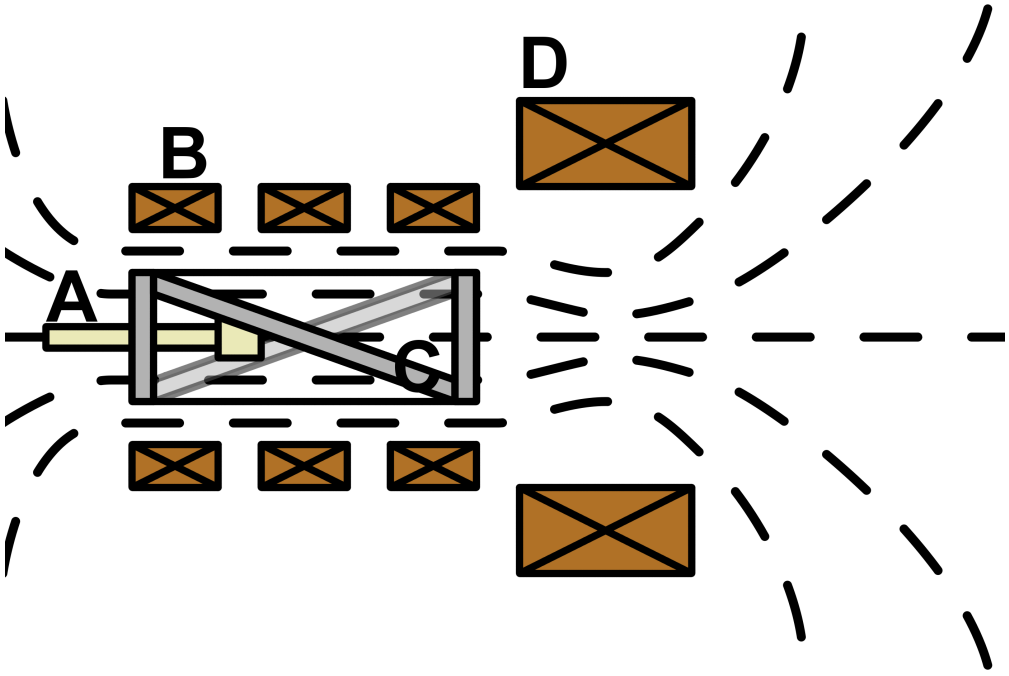

FIGURE 1.3: A helicon source with downstream nozzle (D)

At present, the APL is equipped to study helicon sources in a variety of configurations and power levels. These systems allow for high-density plasma with good shot-to-shot consistency. The helicon plumes created show good charge distributions, velocity, and response to magnetic fields. Researchers in other locations have shown additional successes not focused on at the APL. The VASIMR project, owned by Ad Astra, has successfully produced steady-state helicon beams

on several occasions [18] [19], proving that continuous beaming is possible. Other testing has shown that a high generation efficiency is possible, reaching 50% in certain configurations [20].

Because of these properties, helicon beams make an appealing alternative to microwave or laser systems on the generation side. They have comparable travel distance, generation efficiency, and operational time, and have the added use of being manipulable via magnetic fields. Unfortunately, these developments have come from research in other fields, and there has been little work done toward drawing power back out of the plasma.

1.3 Collection and Goals

This work seeks to present a simple, effective means of drawing power from a collimated helicon plasma, so as to prove it a worthwhile means of wireless power transfer. This will be accomplished by taking advantage of the charged regions of the helicon beam. The plasma is overall quasineutral, but it has been shown previously that during generation electrons are pushed into the core region [10]. This creates a region of net negative charge, and leaves an outer region of net positive charge. By inserting electrodes into these regions charge can be collected, and a current driven between them, resulting in a power draw (Fig. 1.5). In operation this is similar to the power dissipated over a resistor in a simple RC circuit.

The goals for the collection mechanism are straightforward. The system must, after screening for interference or other effects, be able to draw power from a helicon stream. The device must be capable of accomplishing this without the need for significant external power, and it must do so without damaging itself or other systems. Should these goals be met, the experiment is considered a success.

For real-world implementation, these goals must be expanded. In order to compete with existing WPT the collection system must show high efficiency. It must also be capable of operating for long periods of time or under high energy loads without overheating or overcharging the system. Finally, it must be capable of transmitting power a considerable distance. These goals are

difficult, if not impossible, to test in current laboratory settings, and their metrics for success will vary depending on the the system's desired use and environment. As a result, these goals will be considered but not specifically measured in this work.

1.4 Contribution of Research

This research serves as an initial venture into collecting power from a collimated plasma, and brings the proposed design from inception to a technology readiness level (TRL) of 3. This will be accomplished through the following experiment:

- Is it possible to draw power from a plasma generated by a helicon source?

Additionally, simulated work will provide insight into the following questions:

- What are the effects of collector device geometry on the three dimensional electric field of said device?
- Is there a saturation point where collector charging will impede device performance?
- Will the inclusion of a magnetic field improve collector performance?

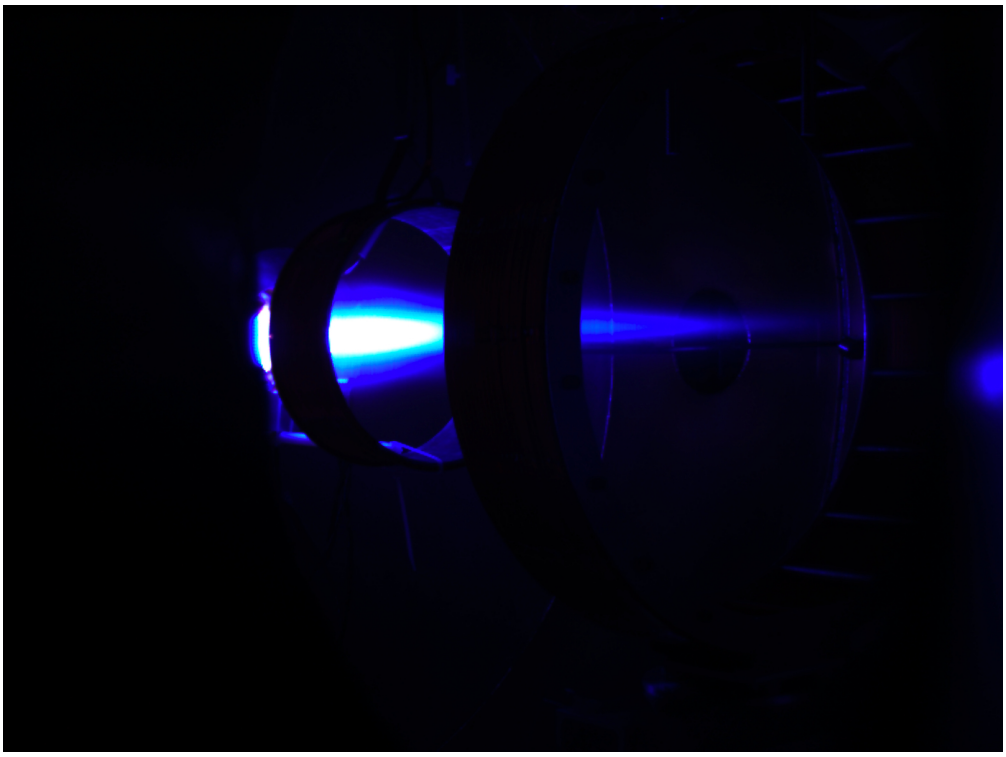

FIGURE 1.4: An HPH thruster with multiple nozzles active [17]

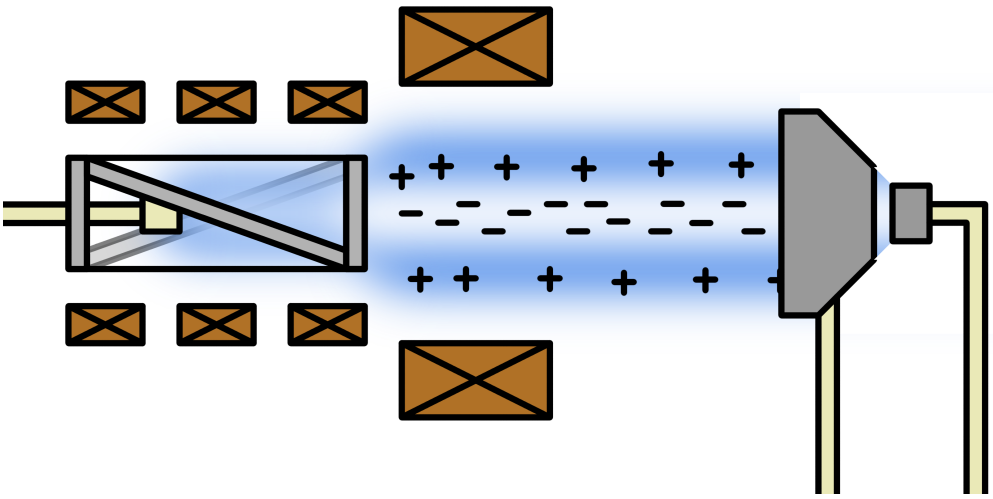

FIGURE 1.5: Diagram of the collection system used in this experiment

Chapter 2

Theory

This section includes the relevant theoretical background for the helicon plasma source. The general properties of helicon plasma generation, and the plasma itself, are discussed in Section 2.1, with focus on properties relevant to this work. Section 2.2 and 2.3 focus on utilizing the inherent charge separation and magnetic field alignment, respectively, of a helicon plasma as they are of particular interest for power collection and transfer.

2.1 Plasma Generation

As stated in Chapter 1, a helicon plasma source was chosen as a beam generation mechanism. This was experimentally preferable as there is significant background within the research group for operation of a helicon source, and the one used here had been previously characterized. The helicon source is preferable in implementation as it is capable of producing a continuous collimated beam of plasma, ideal for simple, long-distance energy transfer. The specifics of helicon generation are included below.

Helicon waves are a type of bounded whistler waves. In general, whistler waves propagate parallel to the magnetic field of a plasma at frequencies above ion cyclotron frequency (sometimes called the lower hybrid resonance) and below the electron cyclotron frequency [21].

$$\omega_{ci} \ll \omega \ll \omega_{ce} \approx \omega_{pe}$$

These waves are right-hand polarized. Their dispersion relation can be written in a number of ways, such as Eq. 2.1, but can be more intuitively understood from Fig. 2.1.

$$\omega = \frac{k^2 c^2 \omega_{ce} cos\theta}{\omega_{pe}^2} \tag{2.1}$$

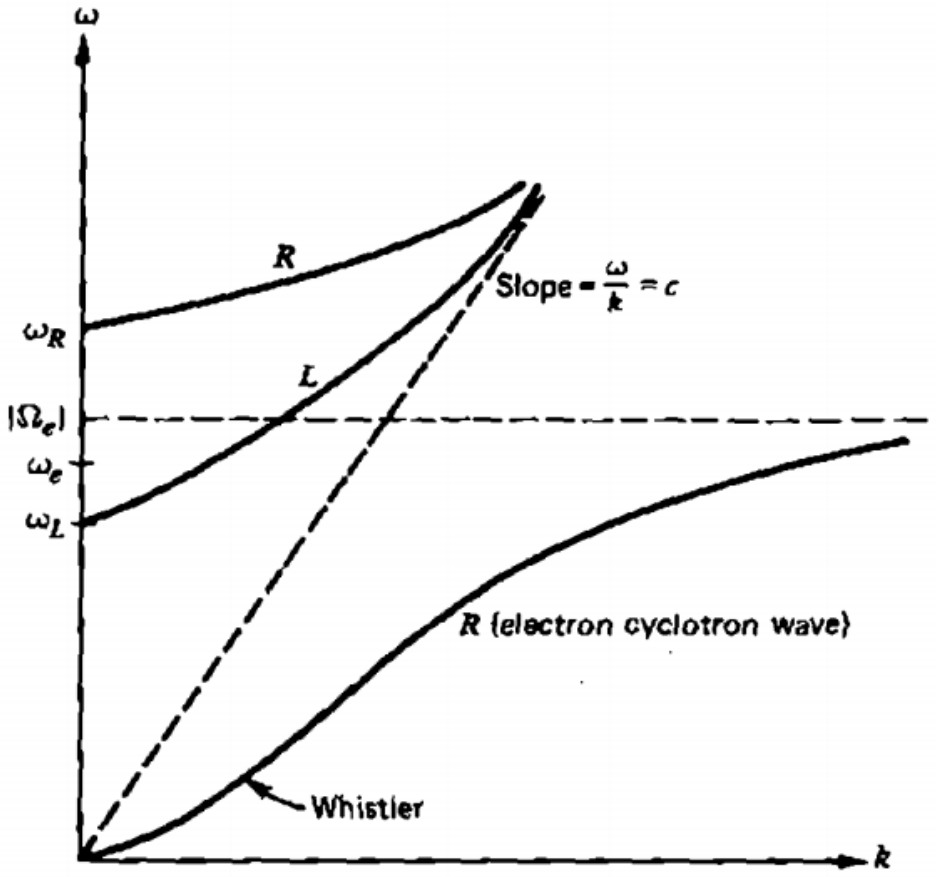

FIGURE 2.1: Dispersion diagram for whistler waves [22]

Helicon waves specifically exist in the lower frequency range of whistler waves, where electrons can be considered by their guiding center motions. They are also bounded, which limits their electromagnetic character [23]. The full dispersion relation derivation will not be included here, but a summary follows.

The helicon dispersion relation can be found from base principles of Faraday's Law, Ampere's Law, and balancing the Lorentz force

$$\nabla \times \mathbf{E} = -\frac{\partial \mathbf{B}}{\partial t} \tag{2.2}$$

$$\nabla \times \mathbf{B} = \mu_0 \mathbf{j} \tag{2.3}$$

$$\mathbf{E} = \frac{\mathbf{j} \times \mathbf{B}_0}{e n_0} \tag{2.4}$$

where n_0 is the unperturbed equilibrium density, $\mathbf{B}_0$ is the unperturbed magnetic field vector (assumed to be parallel to $\mathbf{z}$). n, $\mathbf{B}$, $\mathbf{E}$, and $\mathbf{j}$ are the perturbed density, magnetic field, electric field, and current, respectively. These equations then suggest

$$\nabla \cdot \mathbf{B} = 0 \tag{2.5}$$

which is known from Gauss' Law for Magnetism, as well as

$$\nabla \cdot \mathbf{j} = 0 \tag{2.6}$$

$$\mathbf{j}_\perp = \frac{-e n_0 \mathbf{E} \times \mathbf{B}_0}{B_0^2} \tag{2.7}$$

These come from focusing on the guiding center motions, which is established from the low frequency of helicon waves, the fact that the frequency is still well above the ion cyclotron frequency, and the assumption that resistivity is zero. If we then take a perturbation in the standard form of

$$e^{m\theta - \omega t + kz}$$

where m indicates the direction of rotation and k and ω represent the spatial and temporal

aspects of the perturbation. After considerable derivation, which was previously done by Chen [23], we arrive at our helicon-specific dispersion relation:

$$\frac{B_0}{n_0} = \frac{e\mu_0 a}{Z_m}\left(\frac{\omega}{k} + \frac{\omega a}{m Z_m^2}\right) \tag{2.8}$$

where a is the outer radius, and Z_m is determined from the Taylor expansion of the temperature function at a (for helicon systems, $Z_m \approx 3.83$).

For the helicon system used in this work, plasma generation is bounded by the antenna (or more specifically, the quartz tube the antenna is wrapped around) in the plasma generation region, the radius of which provides the value for a in Eq. 2.8. This antenna is a Nagoya Type III antenna, which has a long history of use in helicon plasma generation. These antennas typically come in one of three varieties, depending on their polarity. The m = 0 configuration reflects an antenna with no net polarization, while the m = +1 antenna is right-hand polarized and the m = -1 is left-hand polarized. These orientations can be seen in Fig. 2.2.

While the m = +1 and m = -1 antennas appear to be simple mirrored versions of one another, their electromagnetic properties are noticeably different. The electric and magnetic field profiles can be seen in Fig, 2.3 for a plasma with parabolic density profiles. These fields will remain consistent, aside from rotating as they travel along $\mathbf{B}_0$. This difference is reflected in naturally occurring whistler waves, which are always right-hand polarized [25]. In a vacuum, the current carried from $\mathbf{E}\times\mathbf{B}$ drift (Eq. 2.7) will act along the right-hand wave's magnetic field, but opposed to the left-hand wave's. In an unbounded whistler this will prevent the wave from propagating. In a bounded wave, like our helicon source, this instead leads to a charge buildup in the left-hand wave, causing the difference in field profiles. As a result of this, experiments can find significant differences when comparing right and left-hand antennas in otherwise identical systems. It is worth noting that the above discussion assumes the antenna is aligned parallel to the base magnetic field $\mathbf{B}_0$. In the case they are oriented in opposite directions the resultant wave properties are reversed (i.e: a right-handed antenna pointed opposite $\mathbf{B}_0$ will produce a left-handed wave).

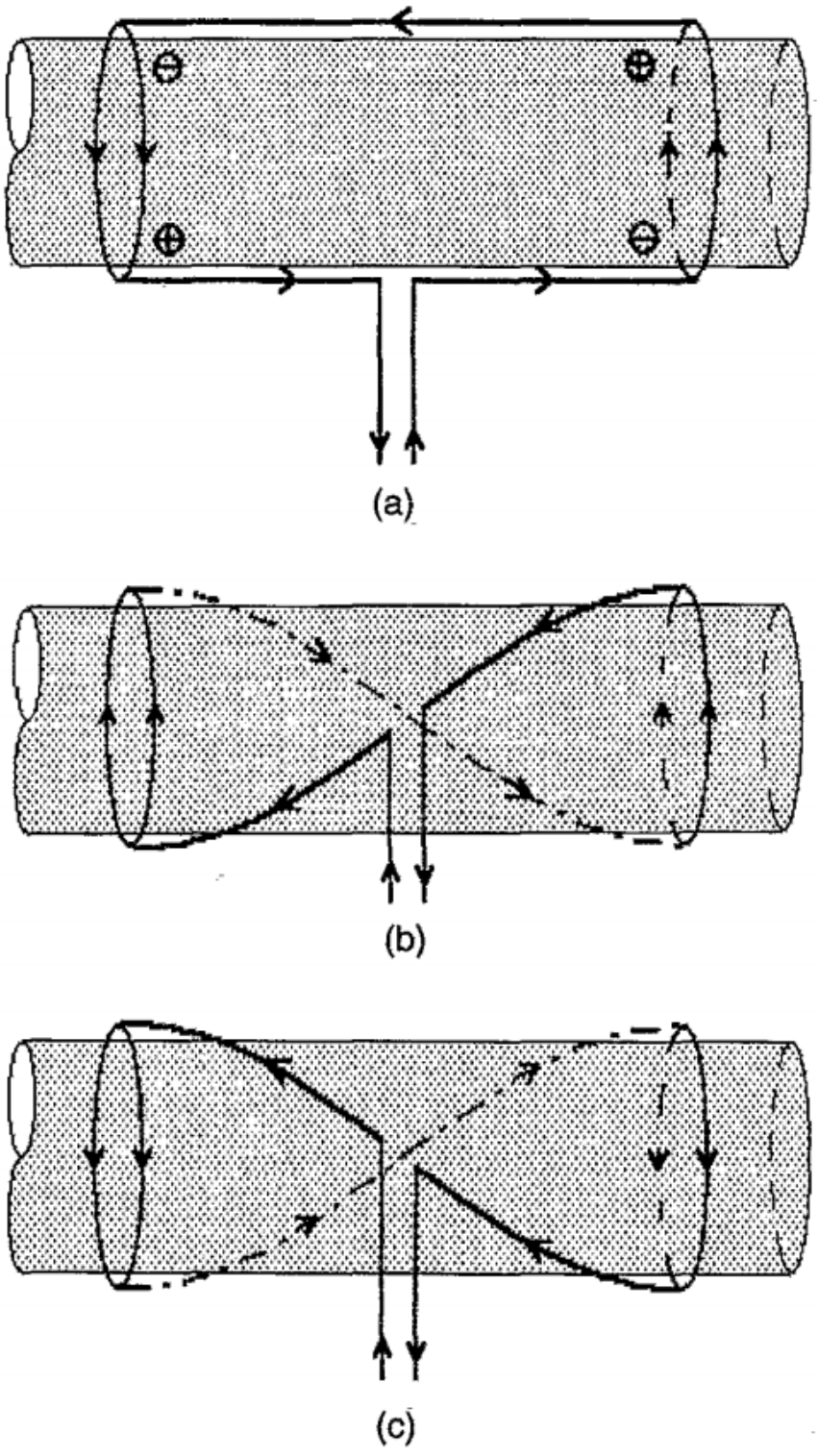

FIGURE 2.2: Nagoya Type III antenna configurations. a) m = 0, b) m = -1, c) m = +1 [24]

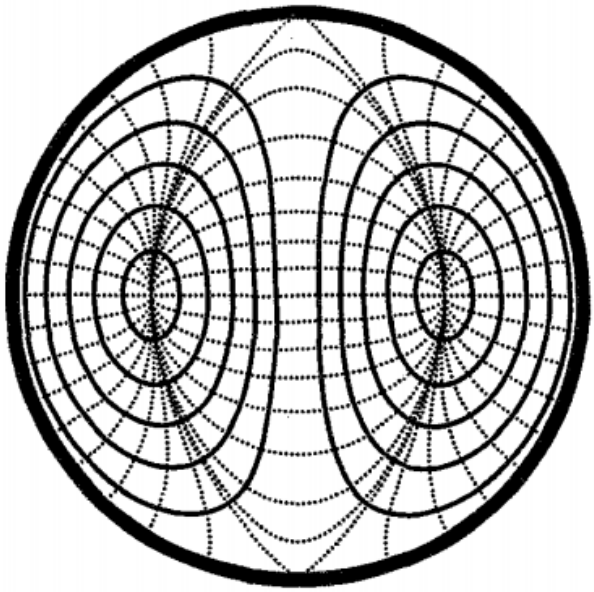

(a)

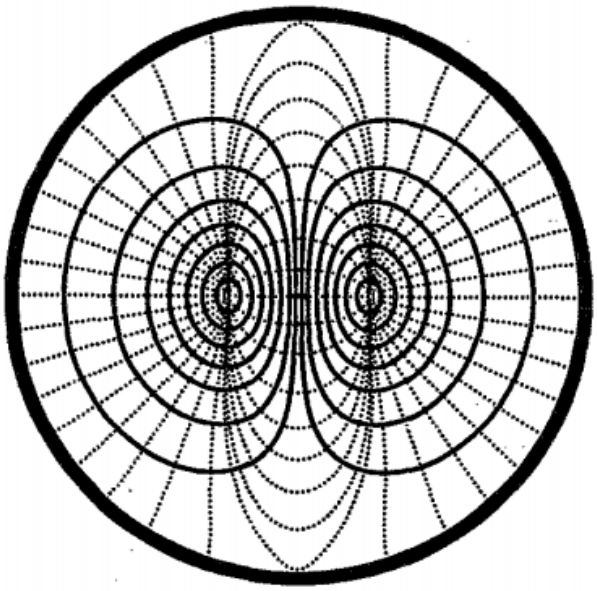

(b)

FIGURE 2.3: Magnetic (solid) and electric (dotted) field lines for the (a) m = +1 and (b) m = -1 Nagoya antennas [24]

Once properly energized in the source region, a helicon plasma can often be identified visually. Many researchers have noted the tell-tale "blue core" of an argon helicon plasma [26]. Other colors have been observed for other elements, such as the often-used xenon, but the core effect remains. While the helicon transition has on rare occasion been observed in plasmas without a distinct core, [27] researchers in the Advanced Propulsion Laboratory have found it to be a consistent indicator of transition in the High Power Helicon system [16]. This dense core is surrounded by a "cloud" or "sheath" of less-dense plasma. The difference in properties of the core and sheath regions provides the base inspiration for this work and is highlighted below.

The core and sheath regions can consist of different, and often conflicting, instabilities, giving helicon systems more potential uses than uniform plasmas [27]. Of particular use is the inherent charge separation in a helicon plasma. Previous work has shown that, though the plasma as whole can still be considered quasi-neutral, the core and sheath regions independently do not follow this assumption. Electrons are typically more concentrated in the core region, [28] [10] with a relatively higher ion concentration in the sheath region. A conceptually analogous, though much simpler, device is the capacitor - a negative charge collection separated from a positive one, making it capable of storing energy. The difference is that a capacitor is discharged as it releases energy, whereas the constant flow of plasma could serve as a consistent source of power. A method of collecting this power using pre-existing technology is discussed in Section 2.2, with experimental verification provided in Chapter 4.

2.2 Langmuir Theory

Though the implementation and goals discussed in this work are novel, the concept of using a plasma to drive current has significant history. The well known Langmuir probe dates back nearly a century, and though its goal was to measure potential rather than draw it, the mechanisms used are essentially the same [29], and serve as the inspiration for this work. This section serves to

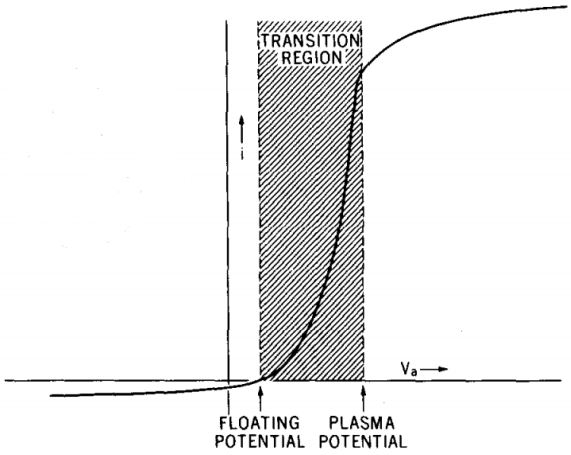

FIGURE 2.4: A typical current-voltage curve created from Langmuir measurements [30]

review the basic theory of Langmuir probes, the history of the diagnostic tool, and its relation to the work described in this paper.

At its most simple, the Langmuir probe is an electrically conductive material inserted into the plasma which will attract or repel charged particles. The attraction or repulsion will then draw a current toward or away from the collection tip, which can be measured. As different voltages are applied to the collection tip, the level of attraction or repulsion will change, resulting in a different flow of current. The collected data can then be used to estimate various plasma properties, including the ion and electron temperatures, the ion and electron currents, the saturation points, and the plasma density. For example, from the measured ion and electron saturation currents, one can work backwards to determine the plasma densities and temperatures.

In practice, it is often easier to find these properties from the trends in the current/voltage comparison. A typical IV curve, then, will be similar to Fig. 2.4. This is often approximated by three best-fit lines, making up the ion saturation region, electron saturation region, and transition region. Of particular interest to this work is the zero point of the transition region, which indicates the floating probe voltage, and the points of intersection, which indicate the plasma potential.

While the plasma potential is, as the name suggests, considered a property of the plasma, the floating voltage and saturation currents can vary for different probe configurations. In the simple

single-tipped probe, where a single conductive surface is held at some voltage relative to ground, the floating voltage is quite important. Some single probes will instead hold the voltage relative to a much larger reference surface placed in the plasma, which can help offset the floating potential. In the case of a double langmuir probe, where two surfaces are placed in close proximity and a voltage is held between the two, only the relative voltages are important, and the floating voltage is largely ignored.

Similarly, the geometry of the probe affects the measurements taken. The difference between spherical and cylindrical tips was seen as early as the original Langmuir probe investigation [29]. Similarly, the size of the probes in question can affect the level at which a collector with saturate [30]. These geometric factors are, of course, known to the researcher who manufactured the probes, and can be accommodated for in data processing.

Of final note is that, typically, the multi-tipped Langmuir probes operate under the assumption that the plasma properties have not significantly changed between the two surfaces. This is valid when either a) the plasma is largely uniform, or b) the tips are very close together. In cases where the plasma properties vary significantly between collection points, assumptions like consistent floating voltages or plasma densities no longer hold, and another method of measurement must be used. However, for a work like this one, which is less concerned with measuring the plasma and more concerned with harnessing it, this difference in plasma parameters is of great use.

It is at this point that the work described here differs from Langmuir diagnostics, even if the physics involved remains the same. In order to maintain a voltage drop across the circuit the two collection surfaces are intentionally placed in regions where the plasma density and net charges differ. As discussed in Section 2.1, a helicon plasma exhibits this well, with a high-density, net-negative core, and a low-density, net-positive sheath. This will allow the two surfaces to naturally come to different floating potentials, and the voltage difference will occur passively.

The other significant difference is one of geometry. Langmuir probes are typically small, often with the intent of minimizing plasma interference. This is, again, ignored here. The purpose of this work is inherently interfering; we are attempting to draw power out of the plasma and use it

for something else. To achieve this more effectively, the collection surfaces will be scaled so as to encompass the majority of the plasma, leaving only enough space to prevent shorting and buildup of neutrals in the collection region.

2.3 Beam Propagation

With plasma generation and collection established, the final problem is connecting the two systems. In order for wireless power transmission to be at all useful, power must be transmitted a considerable distance. Properly aligned laser and microwave arrays are capable of producing a beam with narrow scattering, and since they are pure electromagnetic waves they can maintain this behavior in a vacuum without problem. Plasma beams, on the other hand, are subject to gas dynamics. As a result, a pressure gradient (such as a high pressure plasma in a vacuum) can act against propagation of the beam, and cause a plasma to disperse. The same is true for electric or magnetic fields. A plasma that is not properly contained can be deflected or scattered by a field it happens to pass through. This is easily seen in the Earth's magnetic field; sunlight passes through, but the solar wind is trapped in the magnetosphere.

This effect has also arisen in electric propulsion, though it comes from an entirely different problem. In spacecraft propulsion, momentum cannot leave the full system (i.e. the total momentum will still be net-zero), but it can be split between ejected propellant and the spacecraft. In the case of chemical propulsion this is simple - the propellant has no reason to interact with the spacecraft after leaving. But in electric propulsion, where electromagnetic forces have an effect, additional considerations must be made. In the case of systems like ion engines, spacecraft charging can pull produced ions back toward the spacecraft, causing sputtering and reducing thruster performance, as well as interfering with other systems [31]. This can be neutralized by projecting an additional stream of particles with the opposite charge, preventing the ions from experiencing a pull back toward the craft.

For magnetized systems, such as helicon thrusters, the concern is slightly different. Produced particles will oscillate and travel along the magnetic field lines. This is good for energizing the particles, but detrimental to propelling them. Particles in the center of the magnetic field can find themselves in an equilibrium that propels them outward to infinity, but any which are not along the central axis can either billow outwards or follow their field lines back around the outside of the thruster. This can cause the plasma to expand back around the thruster, leading to a wider, less dense beam and potential system interference. This has been solved, somewhat counterintuitively, by introducing more magnets.

In much the same way that a physical nozzle can improve the performance of a gas thruster, magnetic nozzling has been shown to dramatically improve propagation and separation in helicon systems [14]. Separation of plasma from the magnetic field can be predicted by comparing the plasma's thermal pressure to the external magnetic pressure. This ratio is often called the plasma's β parameter (in this case k represents the Boltzmann constant)

$$\beta = \frac{nkT_e}{\frac{B^2}{2\mu_0}} \tag{2.9}$$

In cases where β is less than one, the magnetic field dominates. This means that the plasma will largely stay attached to field lines, and risks looping back around the source region. But in the cases where β is greater than one the thermal pressure dominates. In this case the plasma expands beyond the limit of the lines, forcing it outward. This thermal motion will create a current in the plasma that induces its own magnetic field, serving as an extension of the base field. In this way a high β system can force a plasma much further away from the source region.

This effect can be amplified through the use of magnetic nozzles. Unlike traditional nozzles, which typically constrict flow through a tight throat, the magnetic nozzles implemented for helicon systems serve more to align the flow. They take advantage of the β term, allowing for thermal expansion but constricting it radially. This forces the plasma to expand axially, accelerating it and aligning its flow. The magnetic nozzle will also typically operate at a lower strength than the base

field, making the β effect more prominent [13]. Simulated results of these can be seen in Figs. 2.5 and 2.6, for systems with one and two magnetic nozzles, respectively. These simulations show the plasma plume to be extended well beyond the scale length of the source system.

The extension of the plasma flow, and the extended magnetic field, also presents an opportunity for flexibility in the system. Microwave and laser transmission systems are limited to line-of-site uses. A plasma system, on the other hand, is capable of not just following, but even linking, non-aligned magnetic source and receiver regions. This allows for curved transmission paths, allowing for easier target tracking, transmission over the horizon, or even obstacle avoidance. A simplified example of these configurations can be seen in Fig. 2.7.

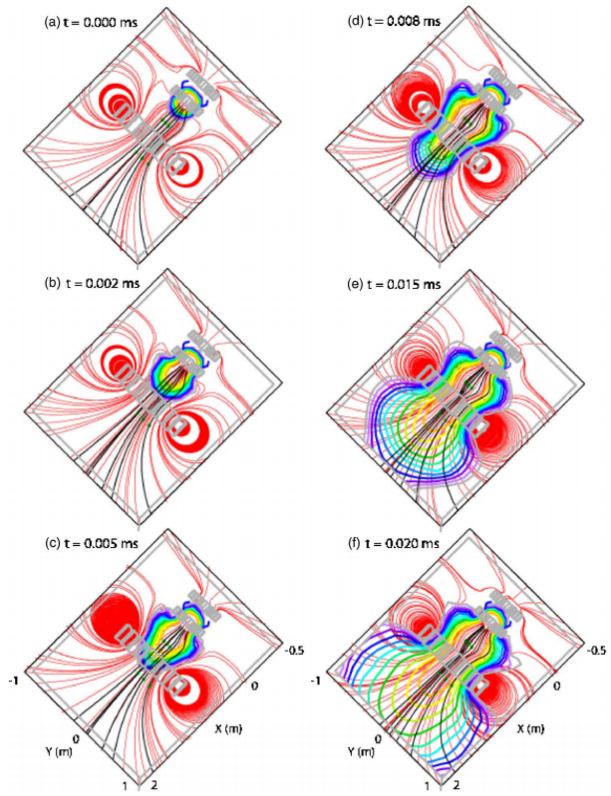

FIGURE 2.5: Beam propagation in a system with one magnetic nozzle [13]

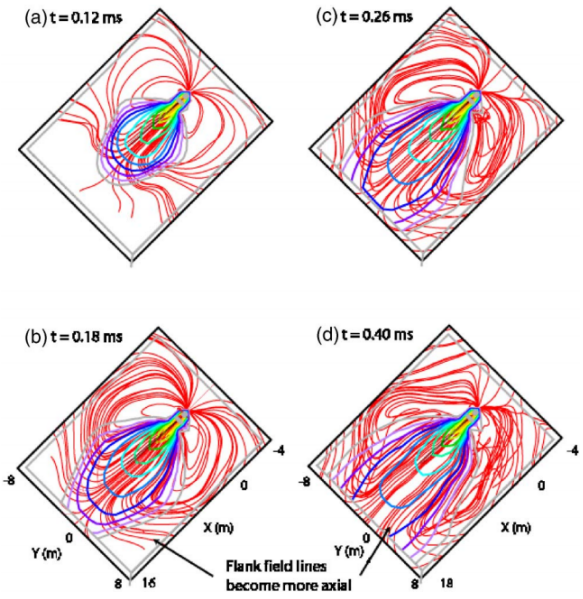

FIGURE 2.6: Beam propagation in a system with two magnetic nozzles [13]

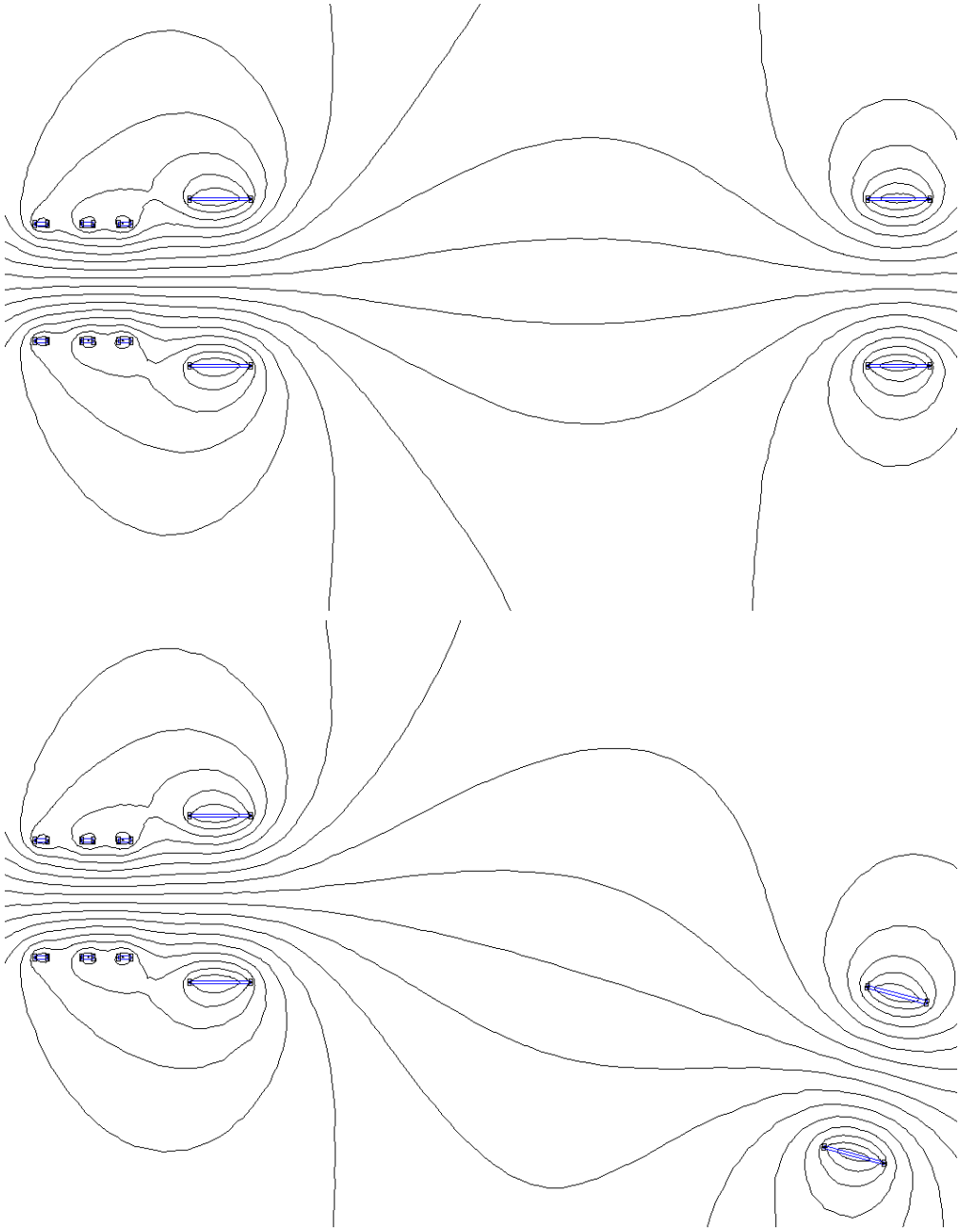

FIGURE 2.7: Magnetic field linkages in aligned (top) and non-aligned (bottom) configurations

Chapter 3

Experimental Apparatus

The plasma WPT experiment consists of a helicon source firing directly into the collection device. Both devices are aligned with the central vacuum chamber axis, and there is a 7 inch separation between the HPH exit and the collector inlet. This configuration can be seen in Fig. 3.1. The following sections cover the specific information pertaining to the experimental setup.

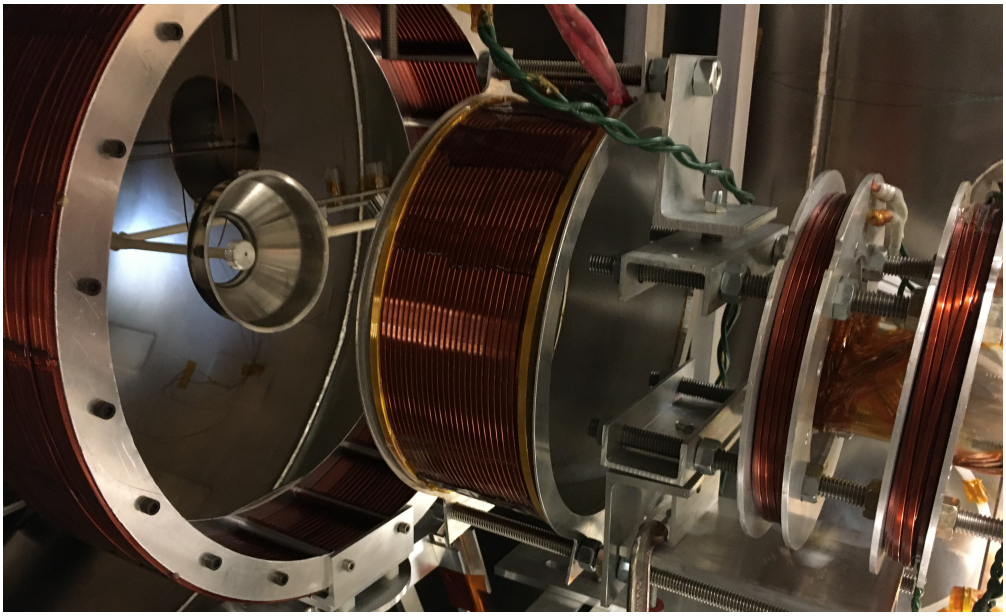

FIGURE 3.1: View of the HPH source and collector, with unpowered additional magnetic nozzle

3.1 Vacuum Setup

To simulate space-like conditions, the WPT experiment is placed in a large cylindrical vacuum chamber, with a diameter of 1.5 m and a length of roughly 2.7 m. This equates to an overall volume of just under 4800 liters. Vacuum is held by a combination of two in-line pumps. For relatively high pressures ($p > 10$ mTorr) pressure is managed using a Varian DS-602 roughing pump. Once this transition point is reached the Varian Turbo-V 551 turbomolecular pump, controlled by a Varian Turbo-V 550 controller, is activated, which pulls the chamber to pressures below 10^{-5} Torr. The arrangement of the pumps can be seen in Fig. 3.2. For pressures above $p = 10^{-4}$ Torr the pressure is monitored by a pair of Pirani gauges, with one placed on the pump line and another on the chamber itself. At lower pressures the chamber is monitored by a Stanford Research Systems GW-100F Bayern-Alpert ion gauge.

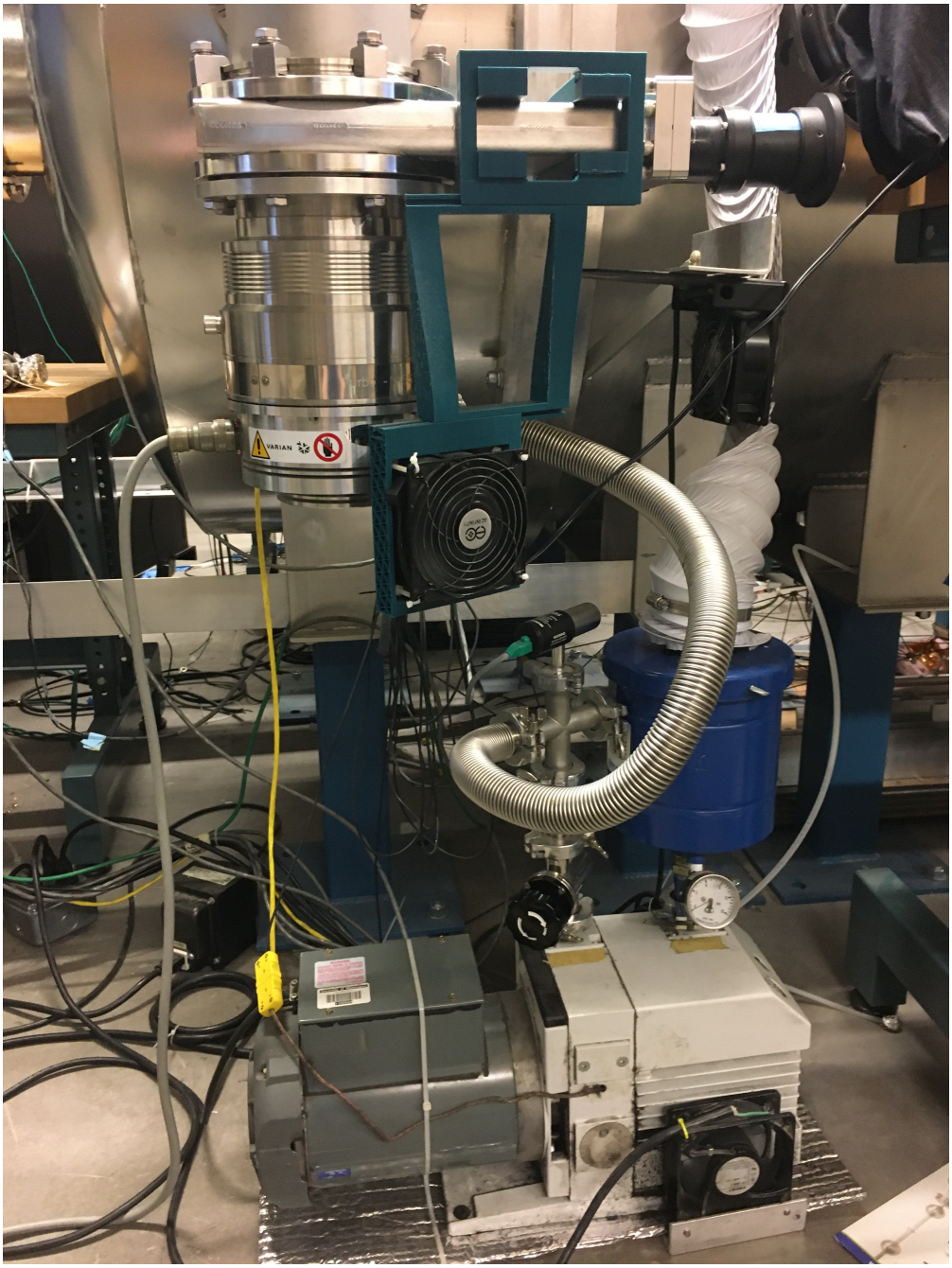

FIGURE 3.2: The turbo pump (top) and roughing pump (bottom)

To ensure space-like conditions, the system was only operated under satisfactory pressure conditions. This is verified by calculating the mean-free path and comparing it to the chamber dimensions. The mean-free path is given in Eq. 3.1

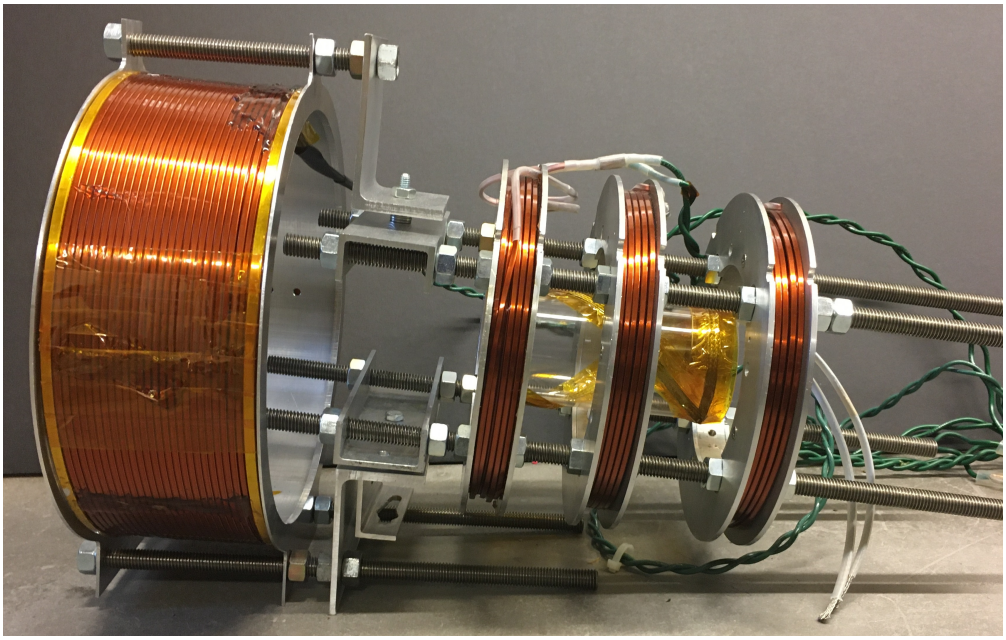

FIGURE 3.3: An HPH source. This source contains an m = +1 antenna, but is otherwise identical to the system described in this work.

$$\lambda_{mfp} = (n_n \sigma)^{-1} \tag{3.1}$$

where n_n is the neutral background density and σ is the ionization cross section [32]. σ has been previously determined to be on the order of 3×10^{-19} m^2 [33]. The upper limit of testing pressure was 8×10^{-6} Torr. Assuming a background temperature of 293 K, Eq. 3.1 and the ideal gas law give a mean free path of 12.7 meters, well above the chamber dimensions. As such, space-like conditions can be assumed.

3.2 Plasma Source

The HPH source, as discussed in Chapter 1, consists of a gas injection/pre-ionization line, a helical antenna, and the surrounding electromagnets. The layout of these assembled components can be seen in Fig. 3.3.

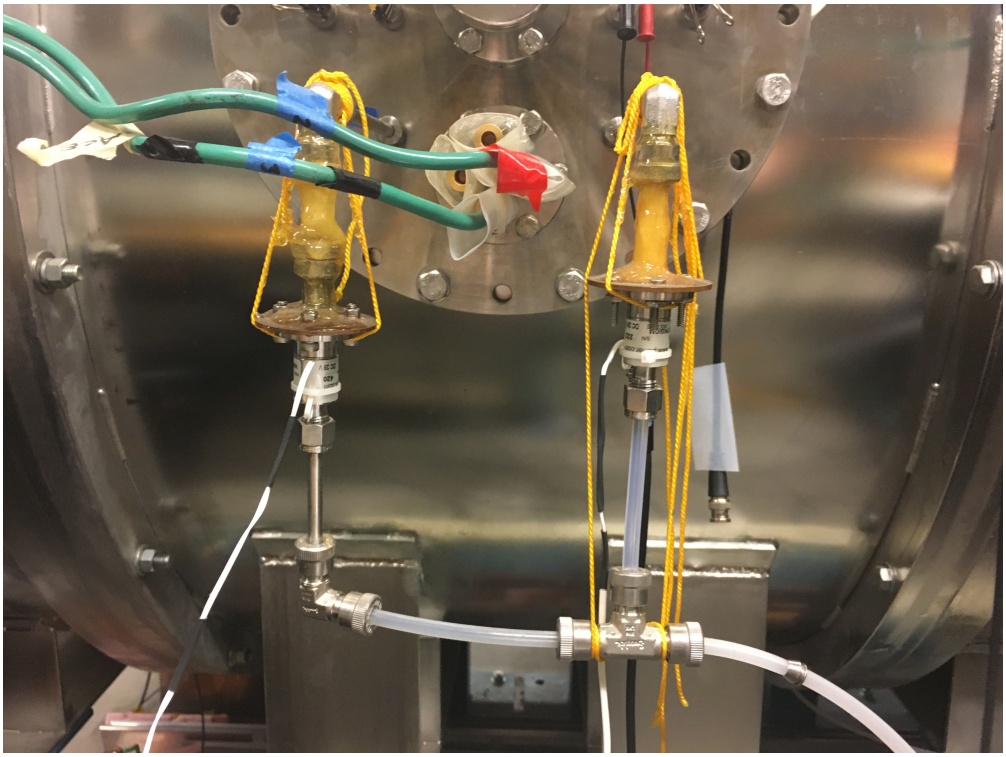

FIGURE 3.4: The valves controlling flow into the vacuum system. For single gun operation only one valve is operated.

These components are driven by an array of external systems, which will be covered in the following subsections.

3.2.1 Gas Management and Ionization

Gas is stored in a standard pressurized storage tank, with line pressure controlled via a manually adjusted needle valve. Gas is released into the HPH system through a Parker 009-1669-900 Miniature High-Speed Vacuum Dispenser valve. This valve, seen in Fig. 3.4, will remain open for a shot time of <12 ms and is triggered through fiber-optics discussed in Section 3.2.4.

Upon entering the source region, incoming gas enters a pre-ionization igniter. This igniter is composed of an alumina tube which directs the plasma to flow through two steel meshes biased to 1.6 kV, similar to the grids of a gridded ion thruster. This bias lasts for only 1 μs and provides seed plasma to be manipulated by the antenna.

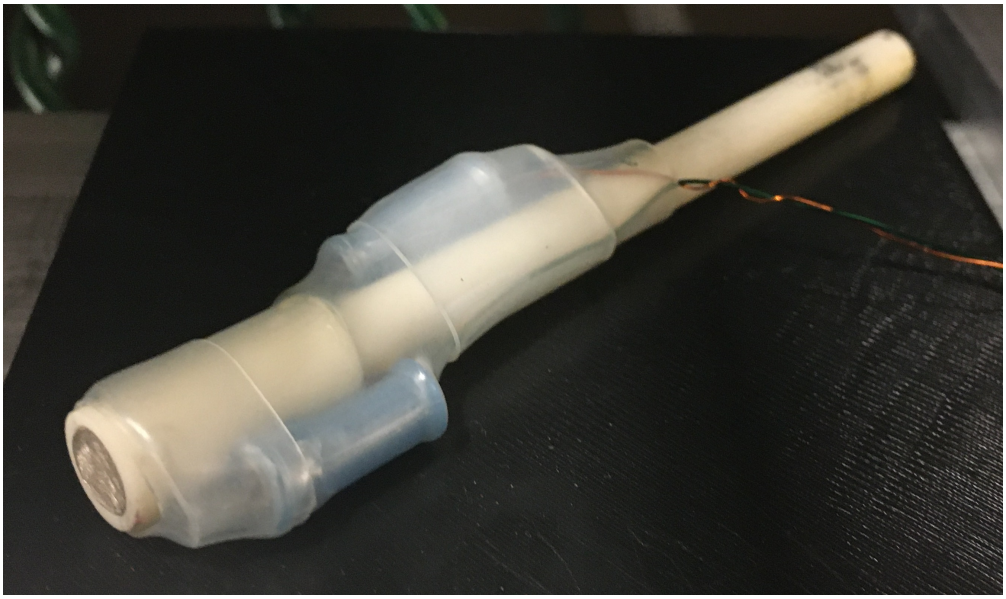

FIGURE 3.5: An assembled HPH pre-ionization igniter

3.2.2 RF Generation and Antenna

As discussed in Chapter 2, energy is primarily coupled to the plasma through a Nagoya Type III antenna. The HPH system is capable of functioning with both m = +1 and m = -1 antennas, though this experiment used only an m = -1 antenna. This antenna consists of a clear quartz glass source tube (15 cm long, 7 cm diameter), capped at one end to prevent back-flow. Copper braids are wrapped around the outside of the tube, with two layers of two half-turns separated and fixed in place through Kapton insulating tape. An example antenna can be seen in Fig. 3.6.

Due to facility limitations, the HPH source is operated in a pulsed mode, with the antenna running for only 200 μs per pulse. The RF pulse is generated by a custom-made solid-state power supply, created in conjunction with Eagle Harbor Technologies. The system consists of an RLC network tuned to drive a current greater than 1.2 kA (peak-to-peak) at a frequency of 625 kHz. The system is capable of safely charging to 300 V, though operation is conducted at 262.5 V. This system is charged manually, but triggered through a fiber-optic pulse.

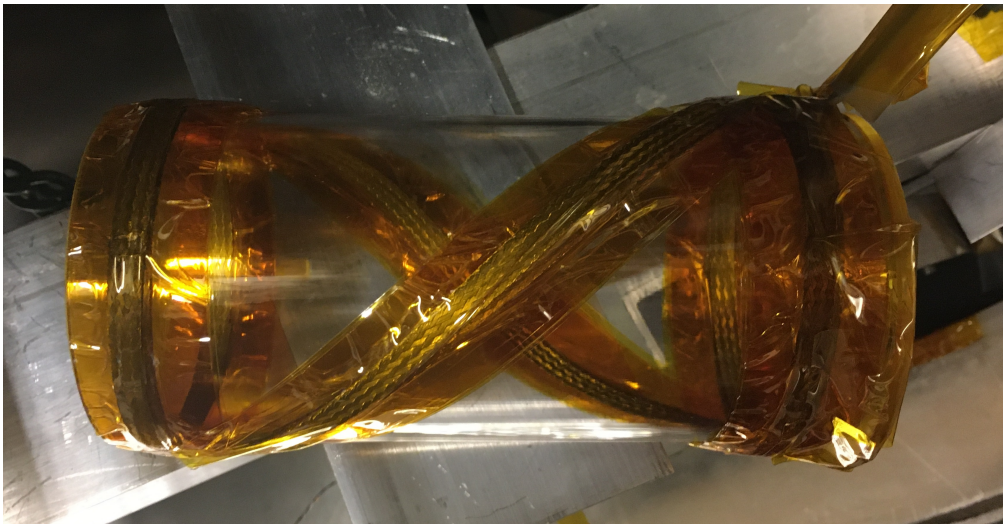

FIGURE 3.6: An antenna (Nagoya m = -1) identical to that installed in the HPH source

3.2.3 Base Magnets and Nozzle

The HPH system generates, confines, and directs plasma through a set of electromagnets, placed coaxially with the antenna and igniter. The system consists of three identical base magnets wired in series to create a consistent base magnetic field in the generation region. This array is powered by an Astex ECR 40V/250A power supply and generates a magnetic field of up to 200 G. A larger magnetic nozzle is placed downstream of the source region which operates on its own circuit. This nozzle is driven by a Hewlett-Packard 60V/50A DC power supply, and generates a field of up to 100 G. System dimensions can be seen in Fig. 3.7. An additional larger electromagnet is installed further downstream, as seen in Fig. 3.3, but was not used in this experimental configuration.

3.2.4 Experimental Control

The HPH source is controlled via a custom Labview 7 interface, which sets timings and parameters for the systems mentioned in previous sections. This interface can be seen in Fig. 3.8. Signals are sent through a National Instruments PXI-1042 modular synchronization system to a set of Eagle Harbor Technologies FTB8-1000 fiber optic transmitters and trigger the chosen systems.

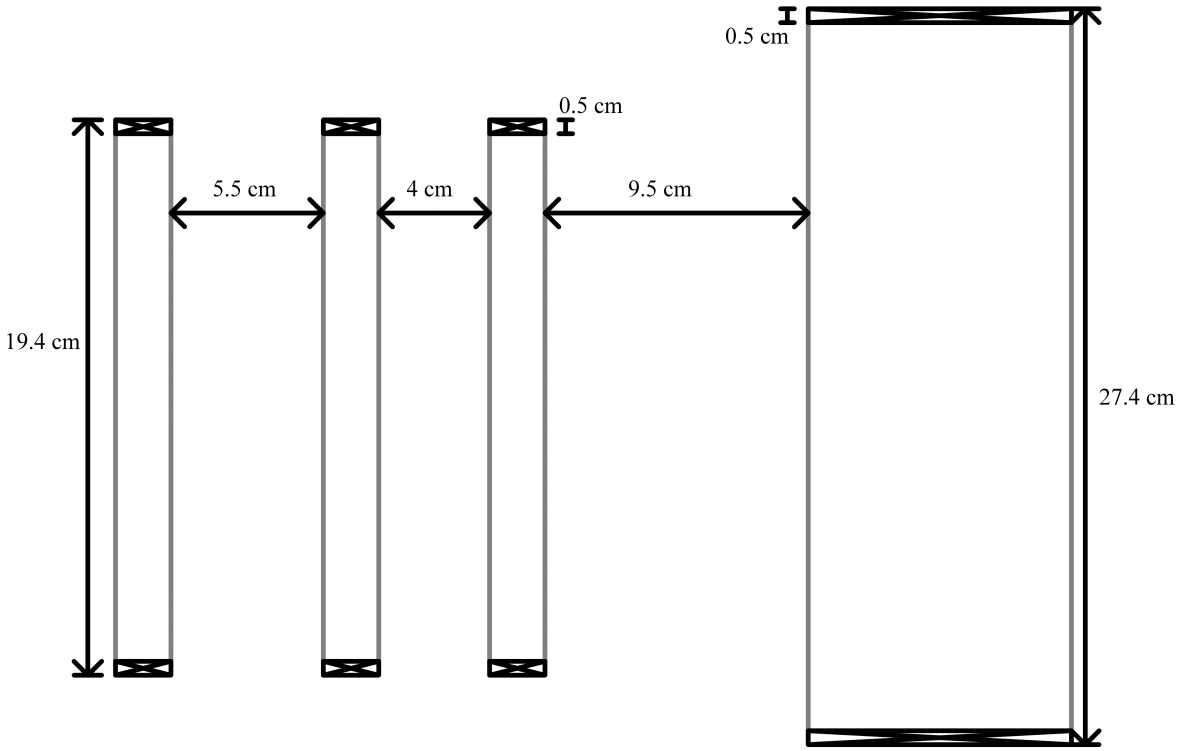

FIGURE 3.7: Dimensions of the HPH magnets without their metal casing

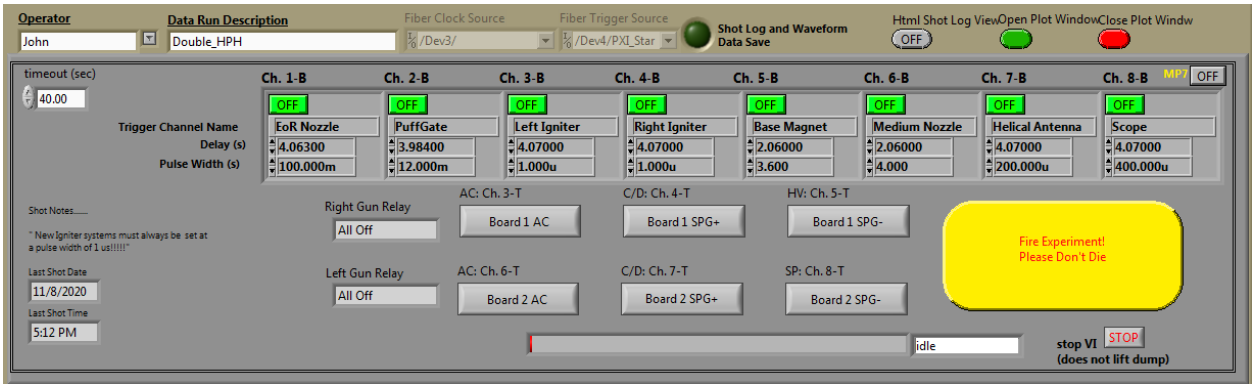

FIGURE 3.8: Screenshot of the HPH control program

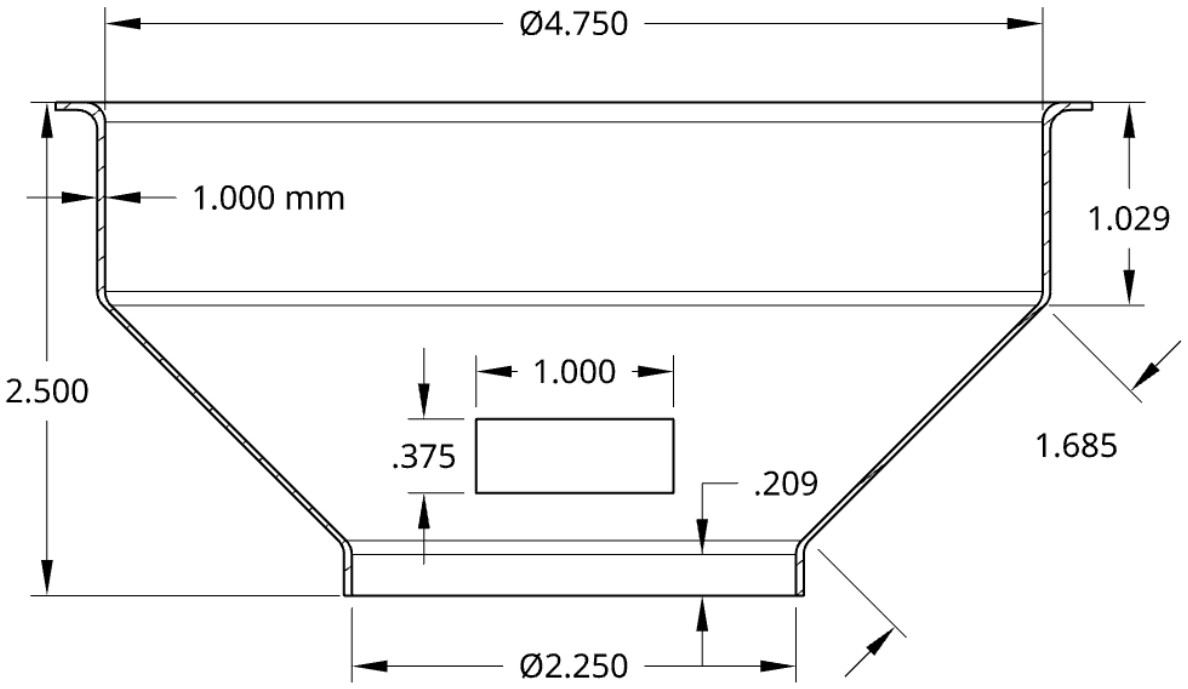

FIGURE 3.9: Drawing of the positive and negative regions of the collector device.

3.3 Collection Mechanism

The collector mechanism was produced to be simple and budget friendly, made from components readily available. The positive collection region is made from a modified 18/10 Stainless Steel kitchen funnel, with an entry diameter of 4 3/4 inches and an exit diameter of 2 1/4 inches, and a height of 2.5 inches after modification. The negative collector region is made from a scrap aluminum disk, 1 inch in diameter and 3/8 inch height. This can be seen in Fig. 3.9.

Wires are routed from each collection surface through vacuum feed-throughs and connected via a resistor. In a powered off state this represents an unpowered, incomplete circuit, but once plasma collides with the collectors current is able to flow over the resistor. This current draw (or, more accurately, voltage drop) is then measured via a Tektronix TDS 3034B oscilloscope, collecting the data discussed in the next chapter.

Chapter 4

Experimental Results

For the purpose of proving the collector to be operational, data was collected for a well collimated argon plasma previously characterized by Vereen [16]. Specifically, this plasma is produced by what he calls the "Left HPH, 1st Magnetic Nozzle" configuration. Additionally, a cloudy, poorly collimated plasma, produced when the system timings were not fully aligned, was tested. This "warm-up" plasma was deemed sub-optimal, as it did not reflect the characteristic blue-shift associated with the helicon transition [27] and therefore its parameters were not fully characterized. Still, it is shown below to prove the system can operate with poorly collimated plasmas, albeit at lower effectiveness. High-speed imaging of typical warm-up and collimated plasma plumes can be seen in Fig. 4.1.

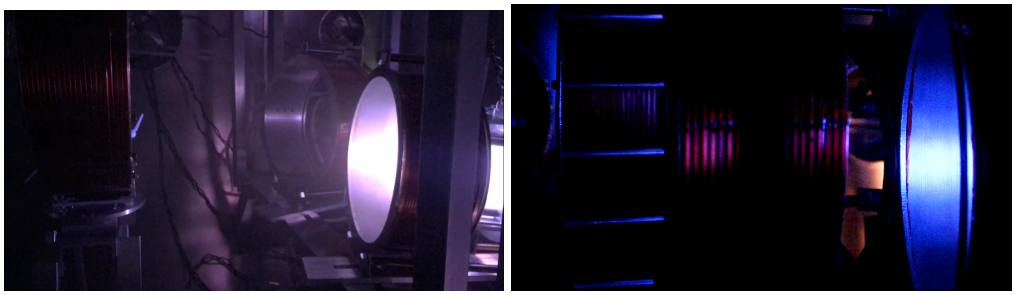

FIGURE 4.1: Comparison of pre-transition (left) and post-transition (right) plasma from the HPH source

Due to limited pumping capabilities the system was operated in a pulsed mode. This means that steady-state operations, while theoretically possible, could not be tested. Considerations for

Experimental System	**Parameter Setting**
Magnet Configuration	
Base Magnet Current	31 A
Base Magnet Pulse Length	3.6 s
Base Magnet Delay	2.06 s
Medium Magnet Current	17.5 A
Medium Magnet Pulse Length	4 s
Medium Magnet Delay	2.06 s
Antenna Configuration	
RF Voltage	262.5 V
Antenna Frequency	625 kHz
Pulse Length	200 μs
Pulse Delay	4.07 s
Igniter Configuration	
Igniter Voltage	1.6 kV
Igniter Pulse Length	1 μs
Igniter Delay Time	4.07 s
Gas Injection	
Argon Line Pressure	16 psi
Gas Pulse Length	12 ms
Gas Pulse Delay	3.984 s

TABLE 4.1: Experimental parameters for the locked in, post-transition helicon experiment

steady-state operation are investigated in Chapter 5. To achieve pulsed operation, equipment was powered on only when relevant to device operation. Final experimental parameters are listed in Table 4.1.

4.1 Pre-Transition Plasma

Because of a number of external parameters, the allowed time for system testing was limited. To align with this, full characterization was not pursued. Instead, potentially interesting configurations were tested. Each was repeated to ensure consistency (typically around 5 shots) and a characteristic data trace was saved. Recorded signals did vary slightly, so a 5% margin of error should be assumed on all measurements. The first configuration pursued was the sub-optimal warm-up plasma, tested over a dummy load consisting of a 1 kΩ resistor. The measured voltage drop across said resistor

can be seen in Fig 4.2. Using basic circuit analysis ($P = \frac{V^2}{R}$) the average power dissipated can be found as 2.21×10^{-5} Watts. As the plasma generated pre-transition does not have significant charge separation, this voltage spike is believed to be the result of a higher particle flux on the larger positive electrode, rather than a charge difference between the two surfaces.

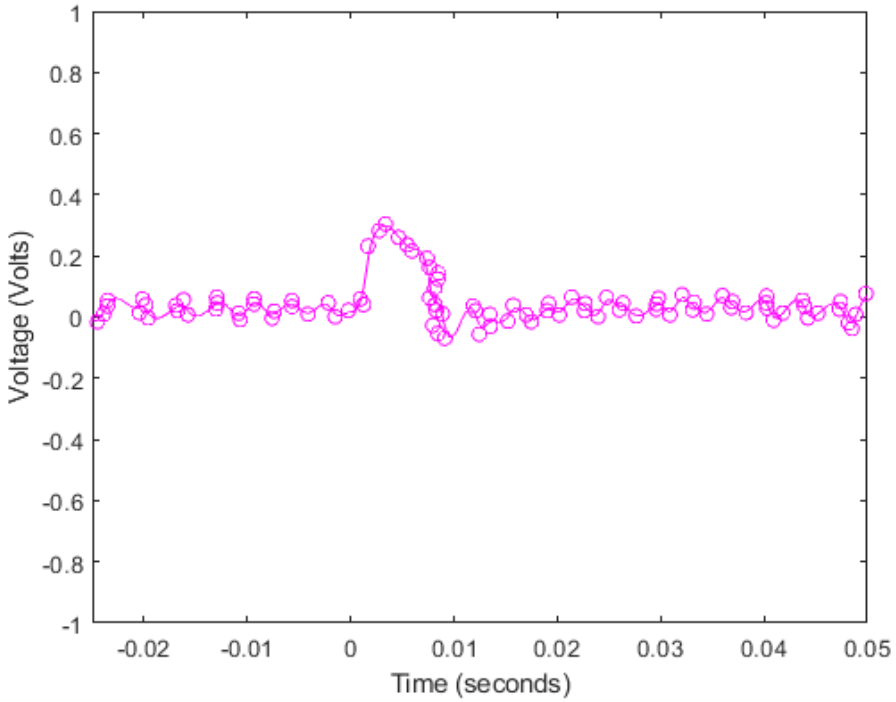

FIGURE 4.2: Measured (o) and smoothed (-) curve for a poorly ionized plasma over a 1 kΩ load

What does become interesting is the results of the same plasma over a different resistor. The 1 kΩ resistor was replaced with a 1 Ω resistor and the system was tested again. The characteristic trace is nearly identical, and can be seen overlaid in Fig 4.3. This indicates that the system is a constant voltage source - that the power output is not limited to a single value, but can instead compensate for different loads on the circuit. In this case, adjusting the load resulted in the average power increasing to 0.027 Watts, a factor of 1000 higher than previous.

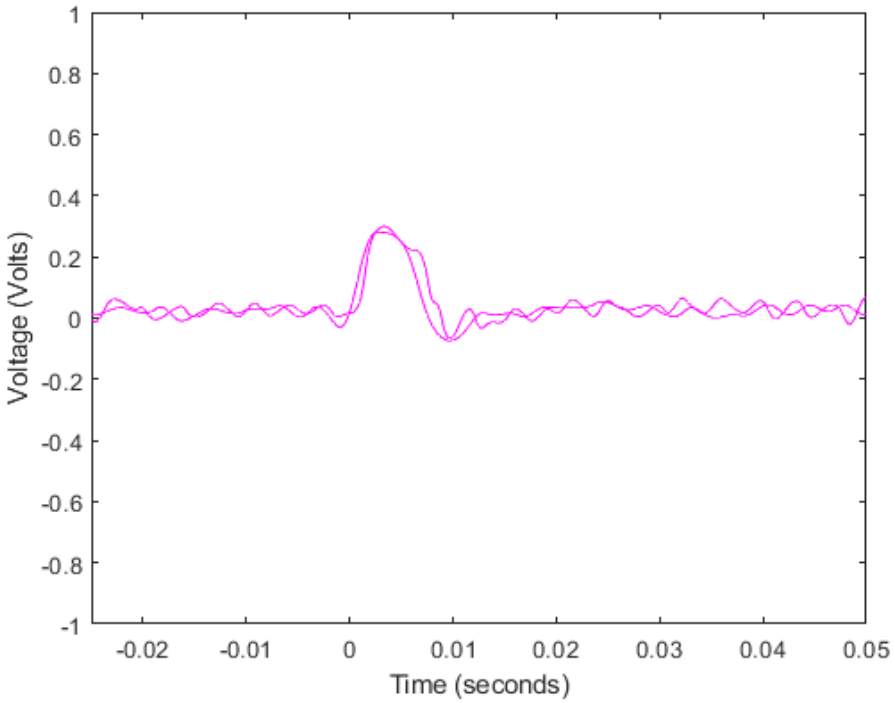

FIGURE 4.3: The nearly identical dissipation curves for a poorly ionized plasma over a 1 kΩ and 1 Ω resistor load

4.2 Post-Transition Plasma

These initial results are promising, but not reflective of the system as designed. Proper collimation is considered necessary for propagating the beam over long distances. Once the plasma consistently transitioned to the helicon mode, the above tests were repeated. Results of the 1 kΩ and 1 Ω tests can be seen in Figs 4.4 and 4.5.

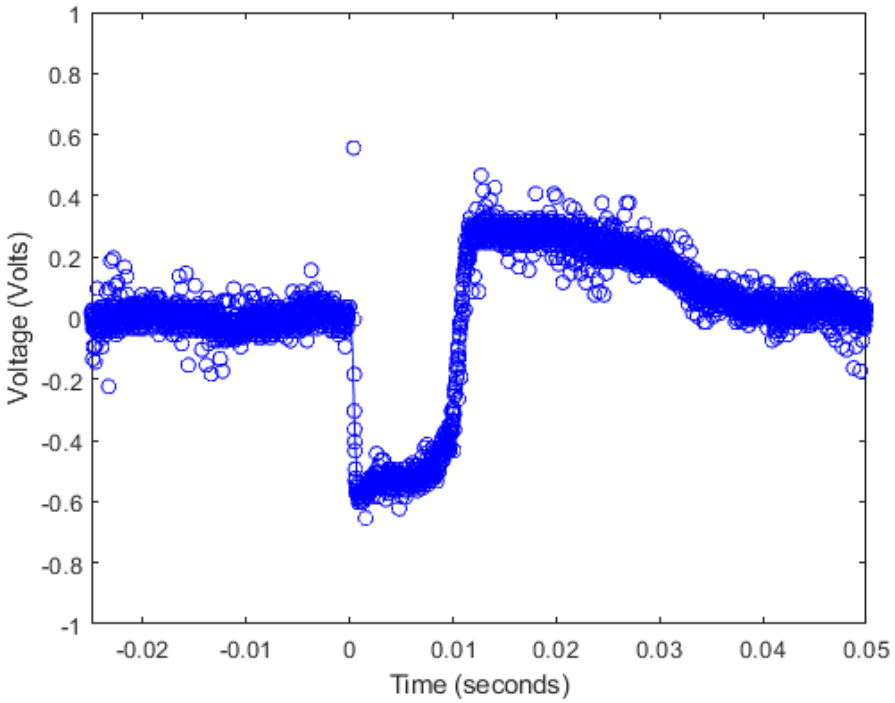

FIGURE 4.4: Measured (o) and smoothed (-) curve for a well collimated plasma over a 1 kΩ load

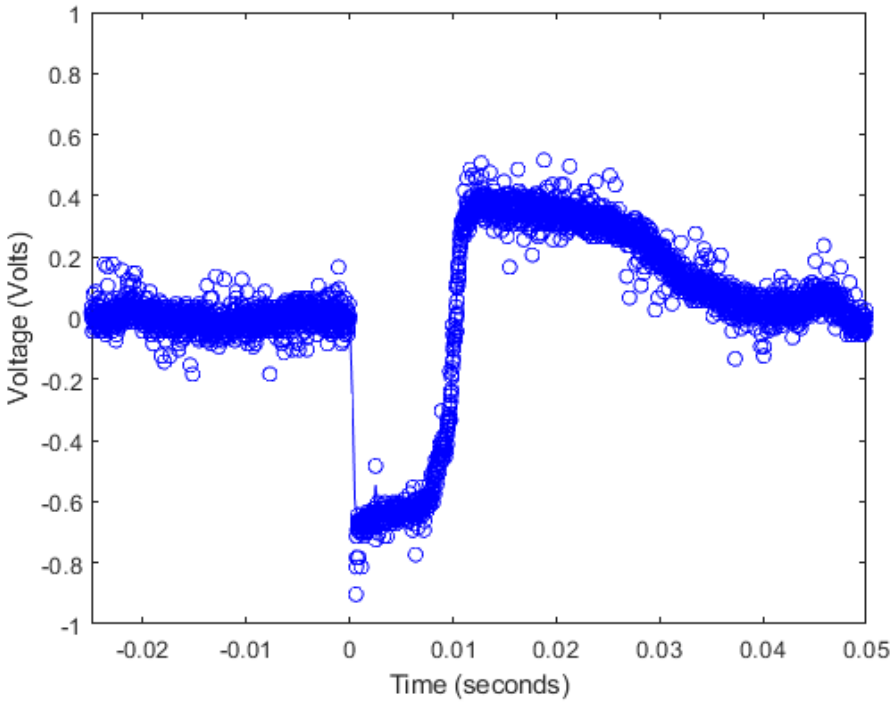

FIGURE 4.5: Measured (o) and smoothed (-) curve for a well collimated plasma over a 1 Ω load

These results do show considerably higher power transmission than the pre-transition plasma, as seen in Figs. 4.6 and Fig. 4.7. The 1 kΩ collimated plasma has an average power of 2.48×10^{-4} Watts. The 1 Ω collimated plasma has an average power of 0.349 Watts. This results in a factor of 12 ± 0.8 increase as a result of the collimation. A summary of these values can be found in Table 4.2.

It is worth discussing the shape of the curve in Figs. 4.4 and 4.5, as they do not indicate the performance expected by the ideal theory presented in Chapter 2. Should the collectors be functioning exactly as expected, the curve occurring between $t = 0$ and $t = 0.01$ seconds would have a positive value, as current would move from the positive electrode to the negative one. This is not a problem for use of the system, as the voltage's sign can be easily rectified, but indicates that this data is affected by the same imbalance as the pre-transition traces. A consistent, negative spike like this indicates that the collector surfaces are overall too small; that the core region is

being collected by both surfaces, and the sheath region is largely missing.

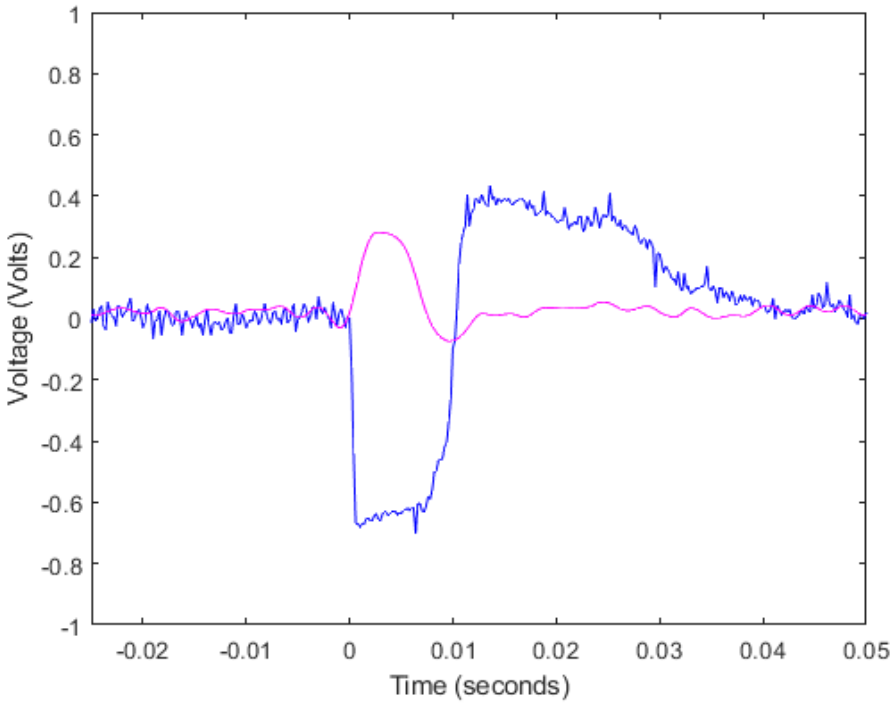

FIGURE 4.6: Comparison of voltage drop for pre-transition (pink) and post-transition (blue) over a 1 Ω load

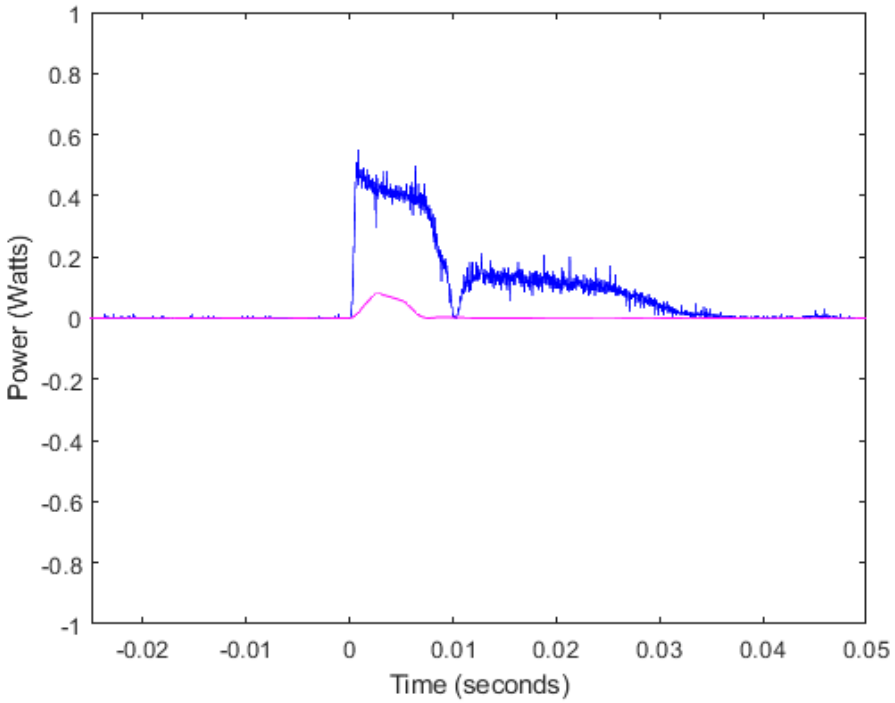

FIGURE 4.7: Comparison of dissipated power for pre-transition (pink) and post-transition (blue) over a 1 Ω load

Resistance	Pre	Post	Increase
1 $k\Omega$	2.21×10^{-5} W	2.48×10^{-4} W	$\times$ 11.26
1 Ω	0.027 W	0.349 W	$\times$ 12.77

TABLE 4.2: Summary of average power draw in various conditions

In the best case results, the 1 Ω collimated system, this system is still highly inefficient, drawing less than 1 W from a 100 kW system. The actual device efficiency is likely higher, however, due to several factors:

- The 1 Ω resistor is the lowest resistance tested, but is not necessarily the lowest resistance possible. Further, these measurements only consider power dissipated by the resistor, but the ringing in Figs 4.4 and 4.5 indicate there is more energy in the system.

- These tests do not include a magnetic nozzle on the collector side, which would allow for better control over particle collisions, as well as increased plasma density in the collection region.

- The collector used has not been optimized, in size or geometry, for the given plasma source. This can be seen in the largely negative voltage curve for the post-transition plasma, which indicates that the core is reaching the positive collector.

Due to both laboratory and external limitations, these factors could not be addressed experimentally. The following chapter serves as an initial, theoretical investigation into these areas.

Chapter 5

Simulated Work

This section provides considerations and investigations of aspects of the experiment that could not be investigated in the given laboratory settings. This includes investigations of varying collector geometries, effects of the saturation expected in steady-state operation, and investigation of magnetic field arrangements for long-distance transfer.

5.1 Effect of Geometry on Electric Field

Future experimental work involving this system will need to pay particular attention to the geometry of both the collector and the plasma stream. In a fully characterized plasma, where the approximate sizes of the core and sheath regions are known, the collector diameters may be easily scaled to match. But the optimal shape of the collection mechanism cannot be defined by its diameter alone. In fact, the geometry explored in Chapter 4 is already known to be sub-optimal beyond the improper sizing, for reasons which will be discussed shortly.

Previous work involving Pulsed Plasma Thrusters (PPTs) has shown that moving to more complicated geometries can produce an increase in performance by nearly a factor of two [34]. Though the purpose of the Pulsed Plasma Thruster is to ionize and accelerate a plasma, rather than catch and deionize one, both are systems consisting of conductive coaxial surfaces meant to hold a voltage difference, so the physics involved are largely analogous. This section serves to explore and expand the methods used in PPT development, and apply them as relevant to the design of the

collector mechanism. In this way, different collector geometries can be explored without the need for production and real-world testing.

To begin this exploration we will assume that the system is operating in a steady-state mode, where variations with time are negligible. In this state the positive and negative collection surfaces are expected to hold a constant voltage (the precise voltage will vary depending on the properties of the plasma used, but that is largely irrelevant to the current discussion). This allows analysis of the collector in the electrostatic regime, and the electric potential between the collection surfaces can be found from Poisson's equation for electrostatics.

$$\nabla^2 \varphi = -\frac{\rho}{\varepsilon} \tag{5.1}$$

where φ is a scalar function representing the electric potential, ρ is the free charge density, and ε is the permittivity. For this analysis we will focus on individual particles traveling through the field, so ρ and ε will be constant (for vacuum, ρ is zero).

Once the electric potential has been determined, the electric field can be found by taking the negative gradient of the potential. In practice this is accomplished through the use of MATLAB's Partial Differential Equations Toolbox. An example of this script can be found in Appendix B.

The purpose of this simulation is to identify regions of high electric field intensity that may interrupt the flow of particles to the relevant collector, and negatively impact device performance. To accomplish this, an idealized version of the experimental device from Chapter 4 has been created (hereafter referred to as the Test Geometry), removing unnecessary flanges and doubling the negative collector diameter to better intercept the core. A cross section of the electric potential for the Test Geometry can be seen in Fig. 5.1, with a full view of the collector itself shown in Fig. 5.2. This configuration will serve as the baseline for simulated comparisons.

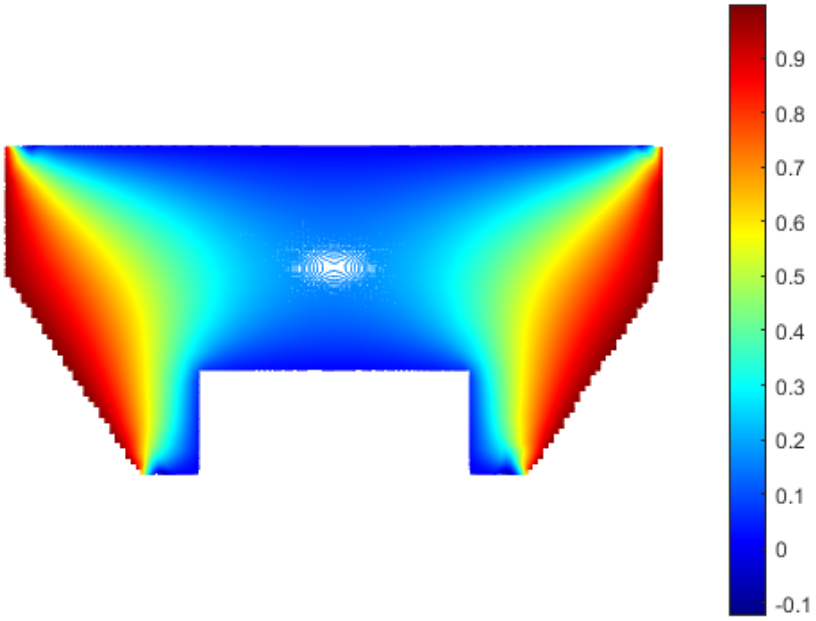

FIGURE 5.1: Cross section of the normalized electric potential for the charged test geometry.

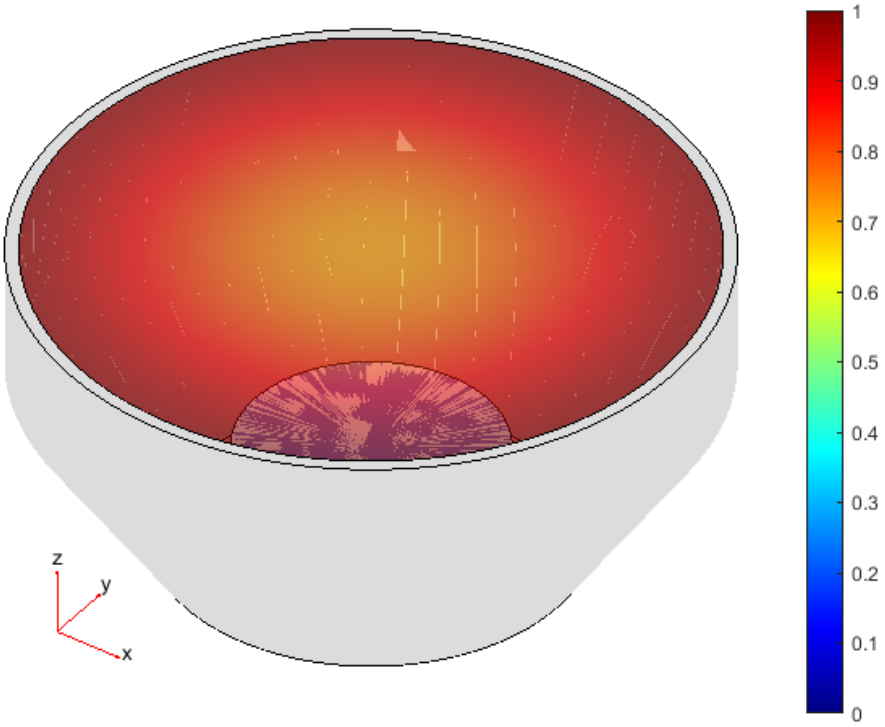

FIGURE 5.2: Normalized electric potential for the charged test geometry.

For comparison, a collector geometry using the same diameter and tapering as the Test Geometry was created using the serrated configuration found to benefit a PPT (hereafter referred to as the Daisy Geometry). This geometry can be seen in Fig. 5.3. The Daisy Geometry has a much smoother potential gradient, and therefore weaker electric field, within its "valleys," indicating good performance in those regions. However, around the pointed edges the field is much sharper, as the electric potential is more highly focused (see Fig. 5.4). This implies a significant repulsion of incoming ions in these regions. The Daisy Geometry does, however, have a higher surface area than the Test Configuration, which would likely allow for improved charging. A cross section showing the difference between edges and valleys can be seen in Fig. 5.5. A schematic of the Daisy Geometry with precise measurements can be found in Appendix A.

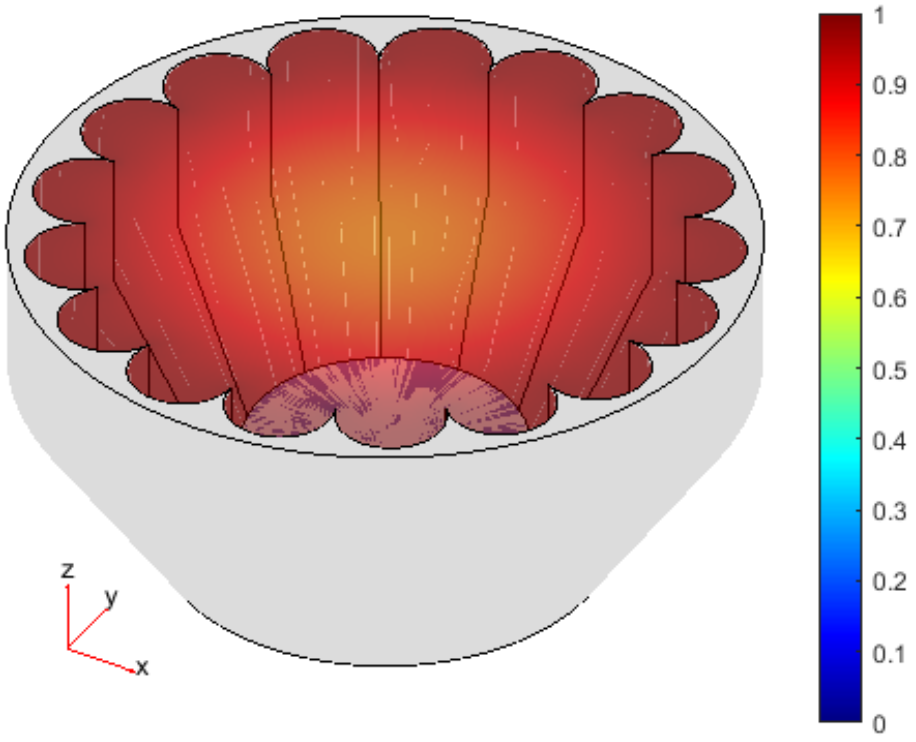

FIGURE 5.3: Normalized electric potential for the charged daisy geometry.

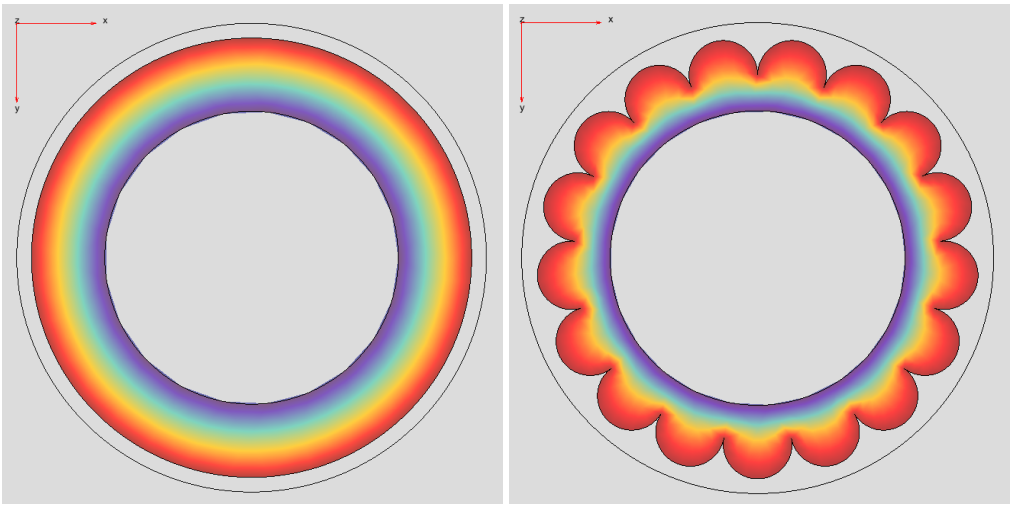

FIGURE 5.4: Effect from the daisy edges on electric potential. (Test geometry left. Daisy geometry right)

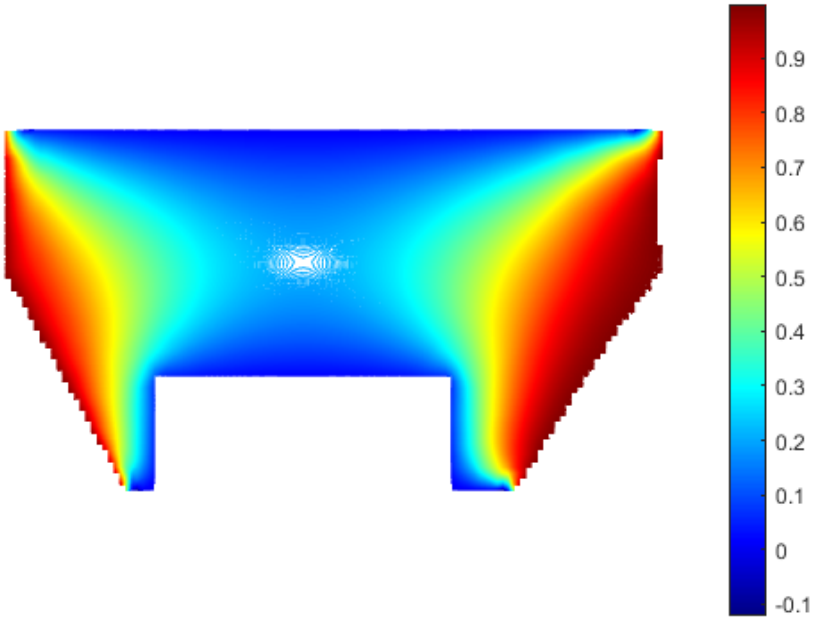

FIGURE 5.5: Cross section of the normalized electric potential for the charged daisy geometry. The left side is an edge, while the right is a valley

Both of these configurations show similar issues in other areas. Most obvious is the extended cylindrical region around the entrance. This region does not provide any significant collection area, as it does not intersect with the bulk path of the sheath. It also produces a large, though weak, electric field region that will redirect particles away from their intended paths. The Test and Daisy geometries also have a flat, cylindrical negative collector surface, which is a poor choice from a fluid mechanics perspective as well as an electrostatic one, for similar reasons to the Daisy Geometry's pointed edges.

Taking these changes into account, we can produce two upgraded configurations. These are referred to as the Conical Geometry (Fig. 5.6) and the Wave Geometry (Fig. 5.7), and each serve to eliminate the initial cylindrical region and avoid sharp edges where possible.

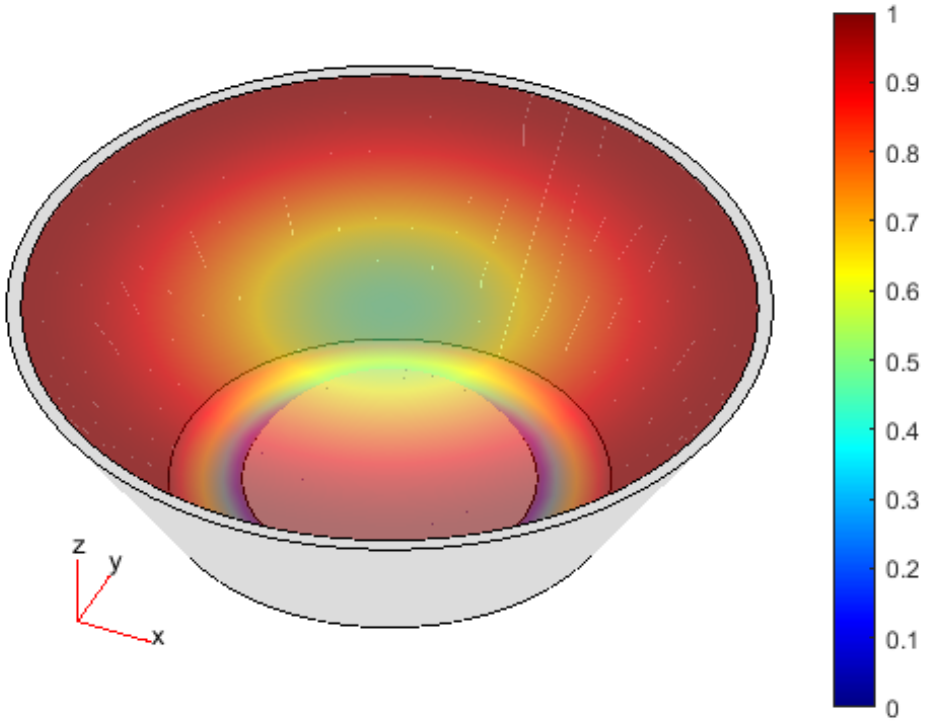

FIGURE 5.6: Normalized electric potential for the charged conical geometry.

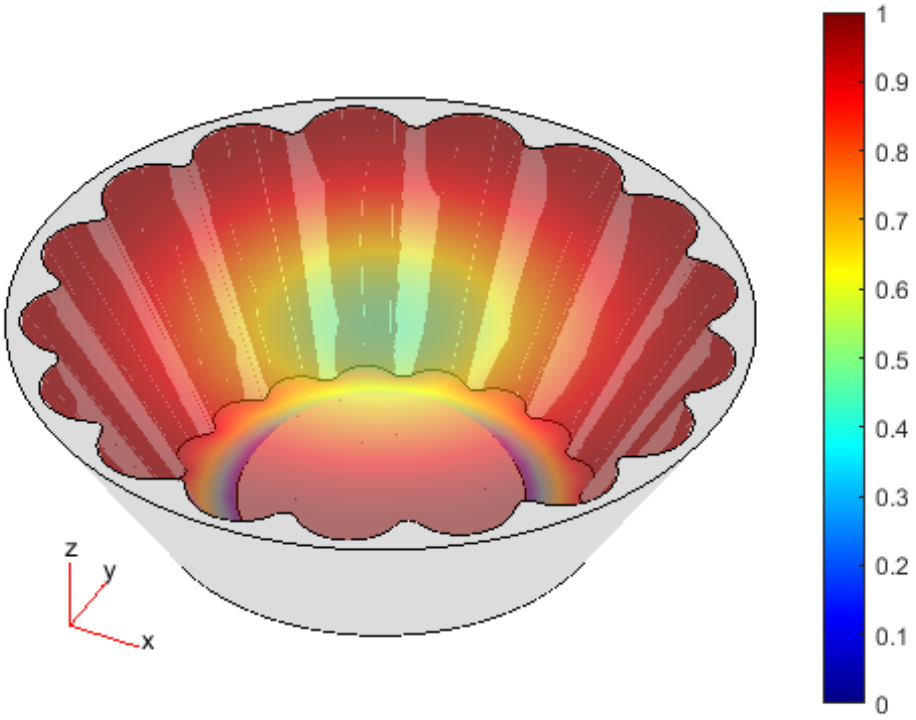

FIGURE 5.7: Normalized electric potential for the charged wave geometry.

These geometries have the same inlet and outlet dimensions as the Test and Daisy geometries, but allow less time for incoming particles to be affected by their fields. Further, the Wave geometry keeps the appealing valleys and increased collector surface area of the Daisy, but removes the problematic edges (Fig 5.8).

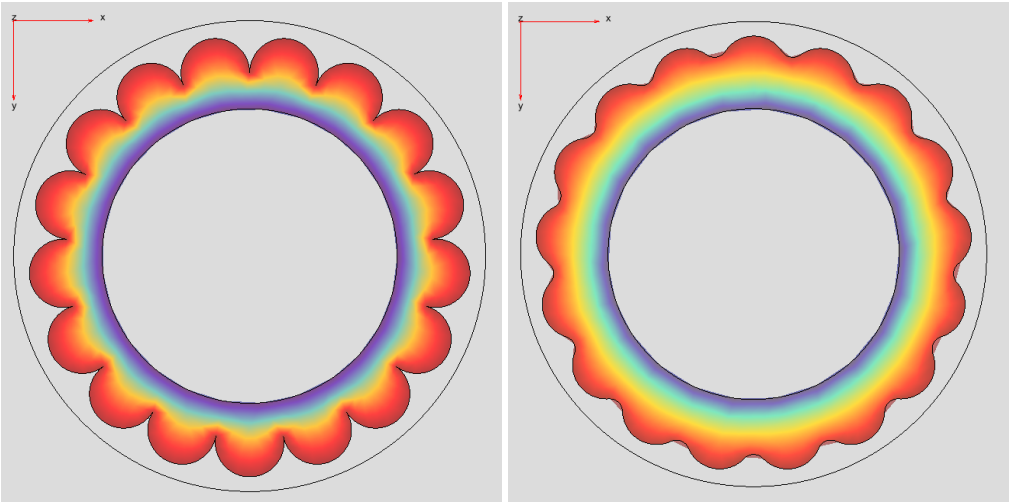

FIGURE 5.8: Comparison of the Daisy (left) and Wave (right) potential fields at their exits

A full list of the tested collector geometries, including schematics, can be found in Appendix B.

5.2 Effect of Saturation on Particle Paths

With the shape of the electric fields determined, the actual strength of the fields is also worth characterizing. To this end, the effect that varying field strengths in a single collector have on passing particles must be simulated. To achieve this, a simple propagator was programmed to supplement the scripts in Section 5.2.1. This script uses initial position and velocity vectors to track the trajectory of a particle of variable mass and charge, updating the path at set intervals based on the surrounding field. An example of a particle's trajectory for the Test Geometry, using a voltage difference of 1 kV, can be seen in Fig. 5.9. This particle is an Argon-I ion traveling at 11 km/s parallel to the central axis, as measured in previous characterizations of the system [16]. The particle enters the collection region 5 cm away from the central axis, putting it in the middle of the positive collector, as would be expected for a properly scaled sheath collector. At this voltage and

trajectory the particle does not experience significant interruption, which is promising for system operation.

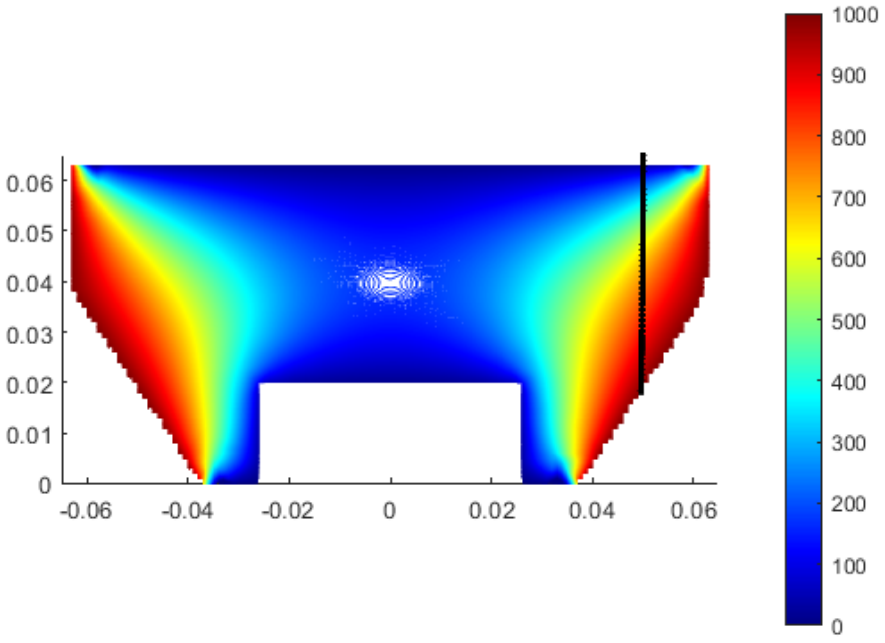

FIGURE 5.9: Path of an 11 km/s Argon ion in the Test Geometry (axis meters, colorbar Volts)

Raising the voltage to a higher value, in this case 10 kV, the particle's path starts to be noticeably changed (Fig. 5.10). This is not a surprising result; a higher potential difference leads to a higher electric field and a stronger force on the particle. But this indicates an upper limit on how much the collector surfaces can be saturated before significant loss of performance. In fact, this particle will miss the collector entirely around 10.5 kV.

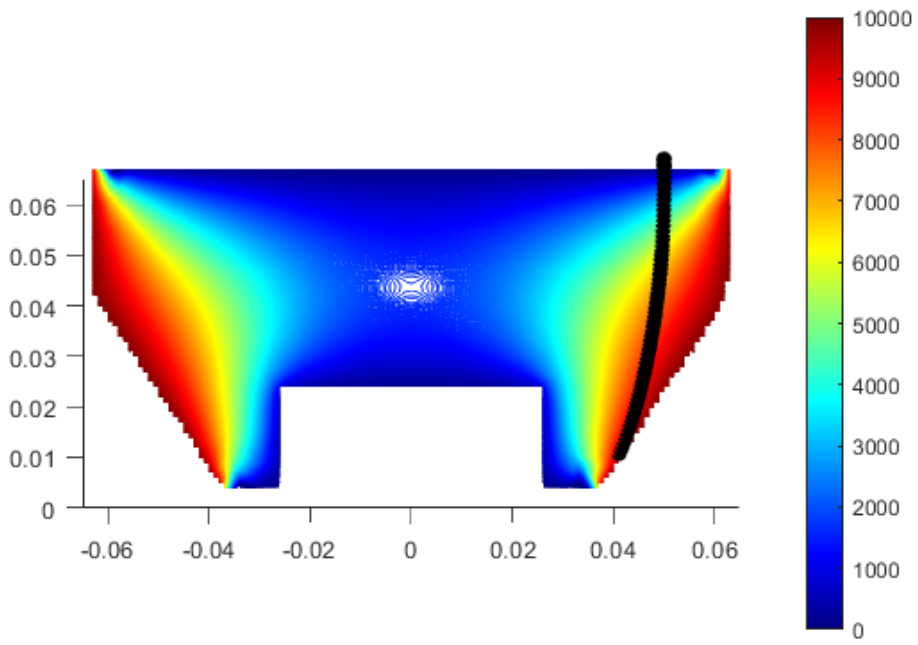

FIGURE 5.10: Path of an 11 km/s Argon ion in the Test Geometry (axis meters, colorbar Volts)

Though the plasma is not expected to reach voltages this high, this particle tracking can provide deeper insight into the effect of collector geometries onto the operation of the device. For these simulations a higher cutoff voltage indicates that the collector geometry has a lessened effect on the particle's path. The improvement between the Test and Conical geometries can be easily seen by propagating the same particle over the new geometry (Fig. 5.11). For this geometry, the particle continues to reach the collector until a voltage of 16.4 kV, a marked improvement.

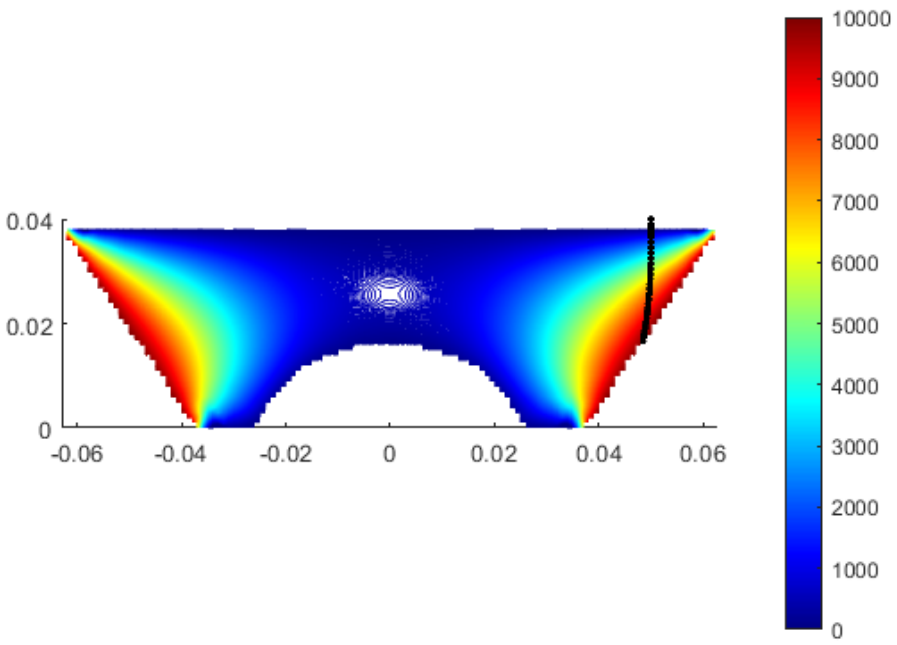

FIGURE 5.11: Path of an 11 km/s Argon ion in the Conical Geometry (axis meters, colorbar Volts)

The full 3-dimensional path of a particle must also be considered. Previous characterization found the bulk plasma velocity to be 11 km/s, but individual ion paths were not characterized. Because of this it is highly likely that the ions enter the collection region with some off-axial velocity as well. The paths of three ions entering the field at 30, 45, and 60 degree angles (with respect to the mid-plane), each with axial velocity 11 km/s, can be seen in Fig. 5.12. The addition of their off-axial velocity causes the ions to have much higher speed than the axially-aligned simulations, resulting in less disruption by the electric field. The saturation voltages for these ions are as follows: 22.7 kV for 30 degrees, 31.1 kV for 45 degrees, and 50.6 kV for 60 degrees.

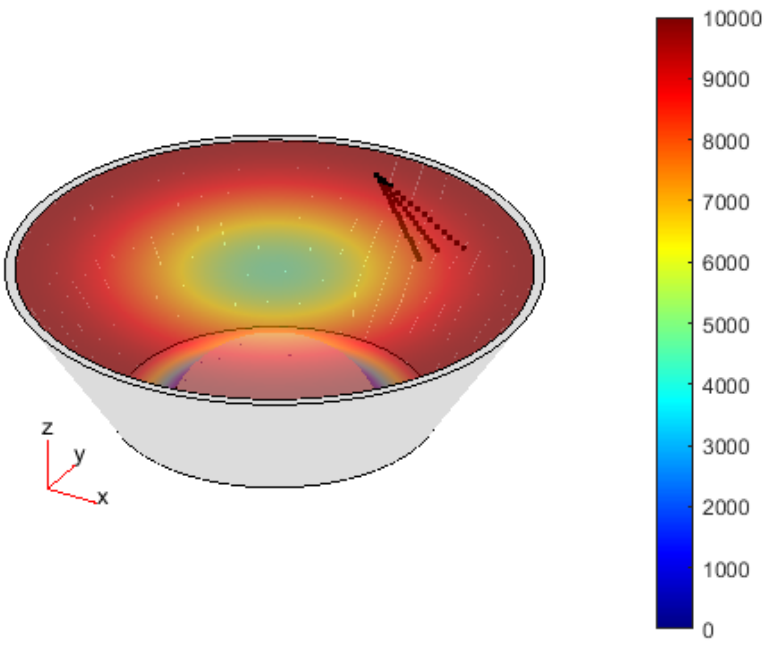

FIGURE 5.12: Path of three ions entering the Conical Geometry with z-velocities of 11 km/s

This becomes more complicated for the wave geometry. When entering near a valley, the saturation voltage for the 60 degree particle increases to 53.4 kV, while the voltage for an ion entering near an edge does not change (though the path distance increases slightly). The difference in paths at 53.4 kV can be seen in Fig. 5.13.

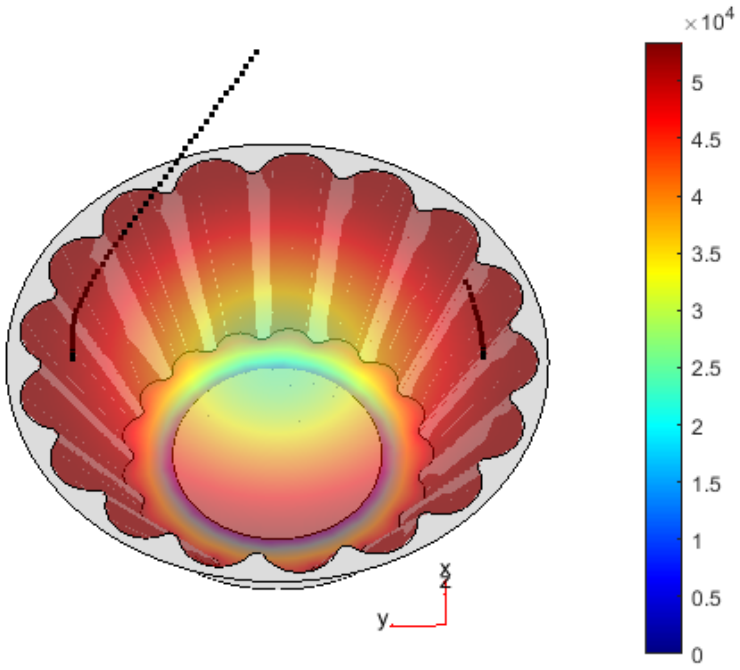

FIGURE 5.13: Path of ions entering near an edge (left) and a valley (right) for the wave geometry

Finally, particle redirection can be mitigated through the addition of a uniform magnetic field, though it is more complicated than the previous results. The spiraling created by the magnetic field can be beneficial or detrimental. For fields on the order of 0.01 Tesla (or 100 Gauss), similar to that used to generate the helicon plasma used in this work, the field is more disruptive; strong enough to affect the particle motion but not to overcome the field. On the order of 0.1 Tesla the magnetic orbit can be seen, but the effect is not necessarily helpful. At the 1 Tesla mark, however, the magnetic field is able to overcome the both the electric field and particle's initial momentum, constricting it to a spiraling motion which is net-parallel to the field's axis. This is beneficial for confining the particles to their desired collection surfaces, but potentially detrimental to the plasma entering the system if the β term is overwhelmed. This effect can be seen in Fig. 5.14.

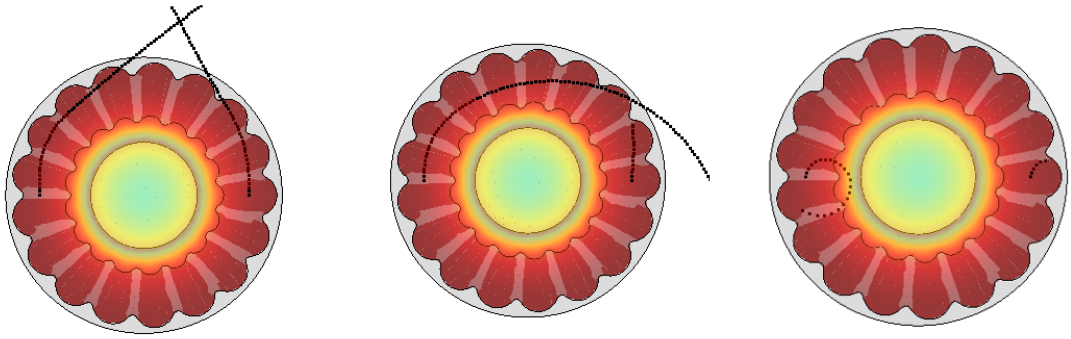

FIGURE 5.14: Effect of an axial magnetic field on ion paths. Initial trajectories and electric field conditions are identical to Fig. 5.13. Field strengths are: 0.01 T (left), 0.1 T (center) and 1 T (right).

Overall these results provide an effective guide for collector geometries, with results favoring the wave configuration. Recommendations for further study are discussed in the following chapter.

The full range of tested particle paths and saturation voltages can be found in Appendix A. The full script used in simulation can be found in Appendix B.

Chapter 6

Summary and Future Work

6.1 Summary of Results

This work serves to provide a groundwork for investigating an alternative system to typical wireless power transfer systems. A helicon source, propagated by a magnetic nozzle, serves as a source device, granting increased operational flexibility than established WPT methods. A concept for a collection device was then laid out based on Langmuir diagnostic theory. This collection device was tested and verified to work experimentally, though performance was sub-optimal. The low performance was been determined to be due to improper scaling of the collector device with respect to the incoming plasma stream.

An approximation of the collection device was then simulated to provide insight into future collector designs. This work indicated that moving from a simple funnel geometry to one with curved edges would improve device performance. Simulated results also indicated that a magnetic field could lead to improvements in the direction and confinement of the incoming plasma beam, further improving device performance.

6.2 Future Work

It is the recommendation of the author that future work focus on a few select areas, so as to further validate the system. These recommendations are as follows:

- Verification of a properly scaled collector device. This would require full radial characterization of the plasma in question, with the transition point between core and sheath determined. This experiment would give further credit to the theory surrounding charge separation in the helicon plasma.

- Characterization of system performance with different collector geometry. This work focused on geometric effects at high voltages in order to better expose geometric trends. In implementation, however, the plasma voltage is unlikely to reach those involved in Chapter 5. Real-world testing is necessary to determine if the differences at low voltage are negligible.

- Testing of the system with an additional magnetic nozzle. An additional magnetic nozzle placed around the collector is expected to assist in connecting the magnetic fields guiding the plasma beam. It would also serve to provide a quasi-uniform magnetic field in the collector, similar to that seen in Section 5.2. This nozzle would require power on the receiver end, however, and could interrupt the plasma if not implemented properly.

- If further experimental testing is impossible, development of a full system simulation. Work here was focused on individual particles and ignored the bulk plasma dynamics. Because of collisions with the walls and neutralization of particles a full fluid simulation was not pursued here, but it would provide further insights into system development.

Appendix A

Collector Schematics and Simulations

A.1 Test Configuration

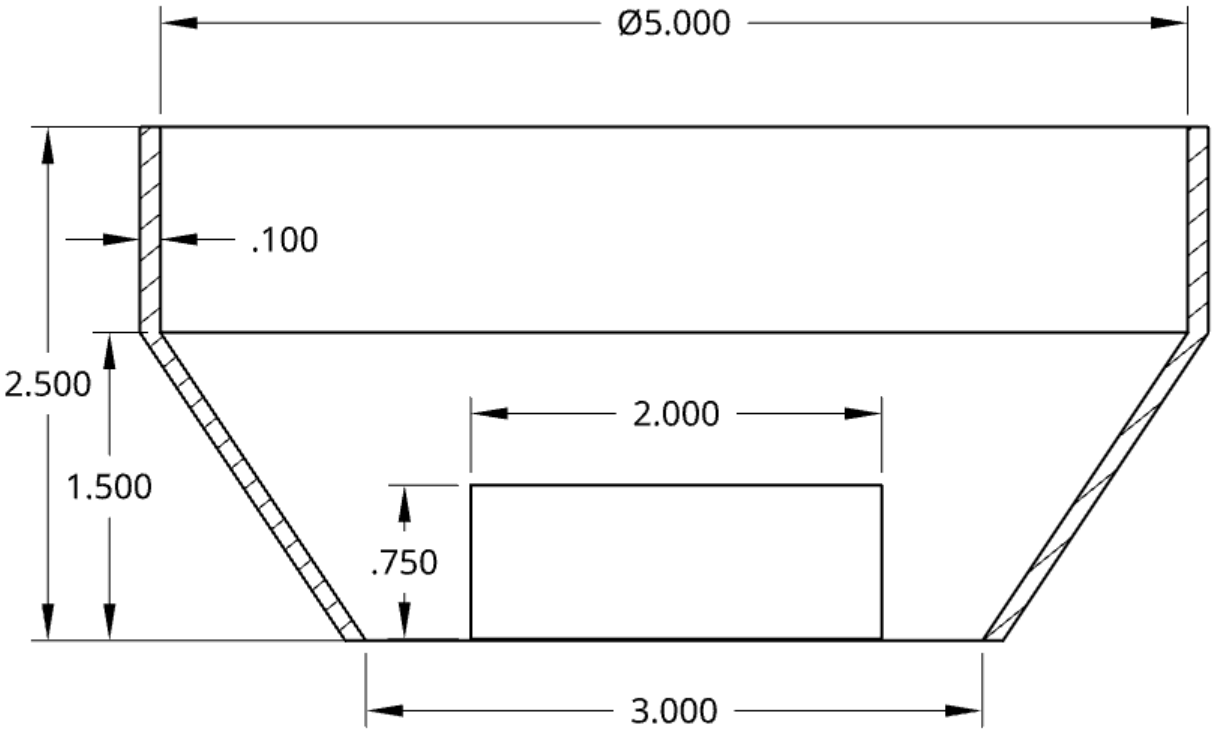

FIGURE A.1: Drawing of the simulated Test Geometry from Ch. 5

radial position	0^o	30^o	45^o	60^o
4 cm	2.7 kV	22.1 kV	41.3 kV	76 kV
4.5 cm	7.9 kV	22.4 kV	38.9 kV	68.5 kV
5 cm	10.5 kV	22 kV	36.5 kV	60.5 kV
5.5 cm	11.5 kV	20.8 kV	34 kV	51.7 kV
6 cm	10.5 kV	17.9 kV	30.8 kV	40.4 kV

TABLE A.1: Cutoff voltages for Argon I ions entering the Test Geometry

A.2 Daisy Configuration

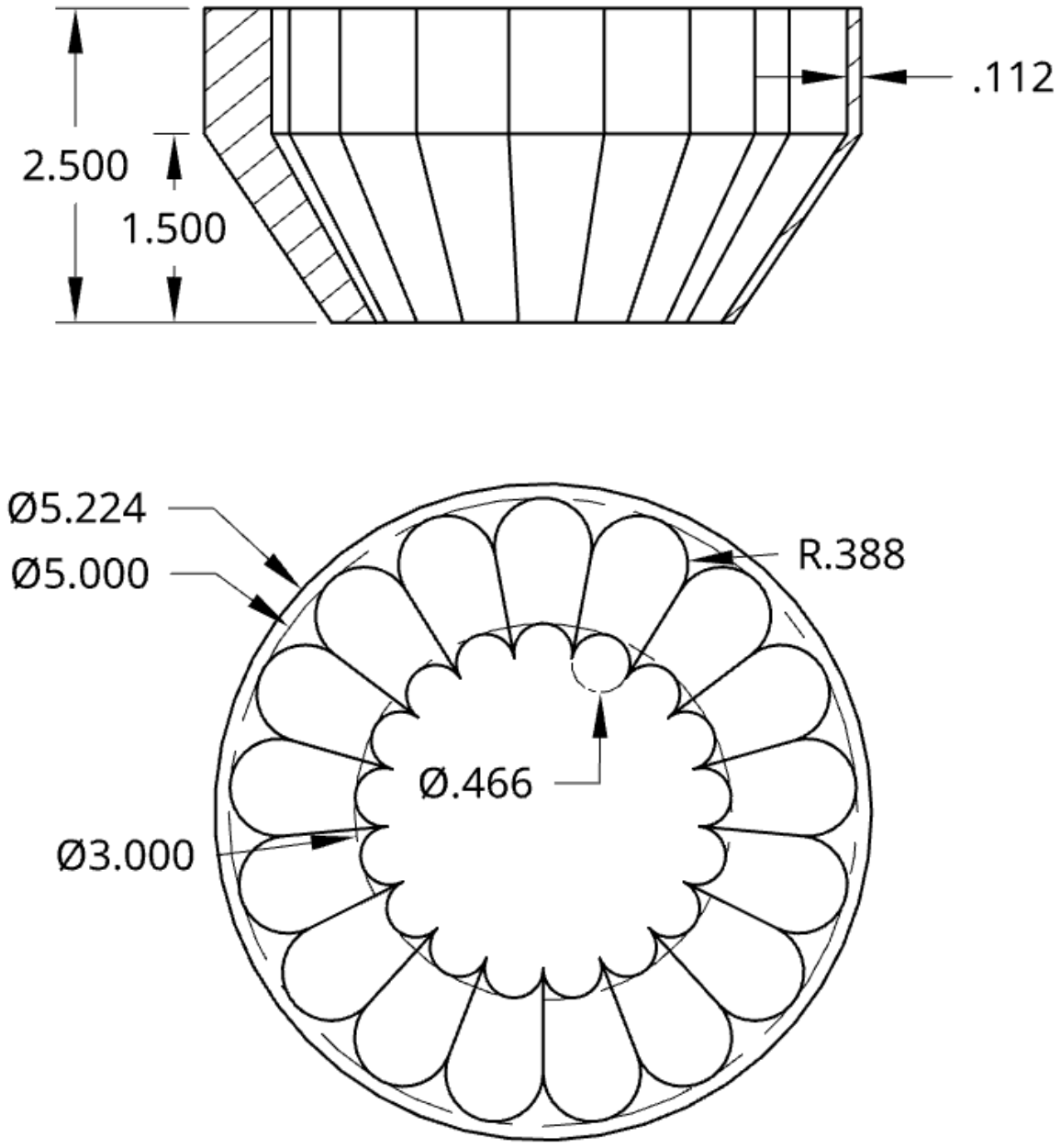

FIGURE A.2: Drawing of the simulated Daisy Geometry from Ch. 5. Negative collector omitted, but identical to Fig. A.1.

radial position	0^o	30^o	45^o	60^o
4 cm	2.5 kV	21.9 kV	40.6 kV	81 kV
4.5 cm	7.1 kV	21.4 kV	37.3 kV	69.5 kV
5 cm	10.2 kV	18.1 kV	35.2 kV	52.7 kV
5.5 cm	13.1 kV	28.2 kV	70.7 kV	205 kV
6 cm	13.1 kV	26.8 kV	69.4 kV	152 kV

TABLE A.2: Cutoff voltages for Argon I ions entering the Daisy Geometry, aligned with a valley region

radial position	0^o	30^o	45^o	60^o
4 cm	7.4 kV	22.7 kV	40.9 kV	76.6 kV
4.5 cm	10 kV	22.4 kV	37.5 kV	67.3 kV
5 cm	6.7 kV	28.9 kV	36.2 kV	56 kV

TABLE A.3: Cutoff voltages for Argon I ions entering the Daisy Geometry, aligned with an edge region. The edge extends just beyond the 5.5 cm point.

A.3 Conical Configuration

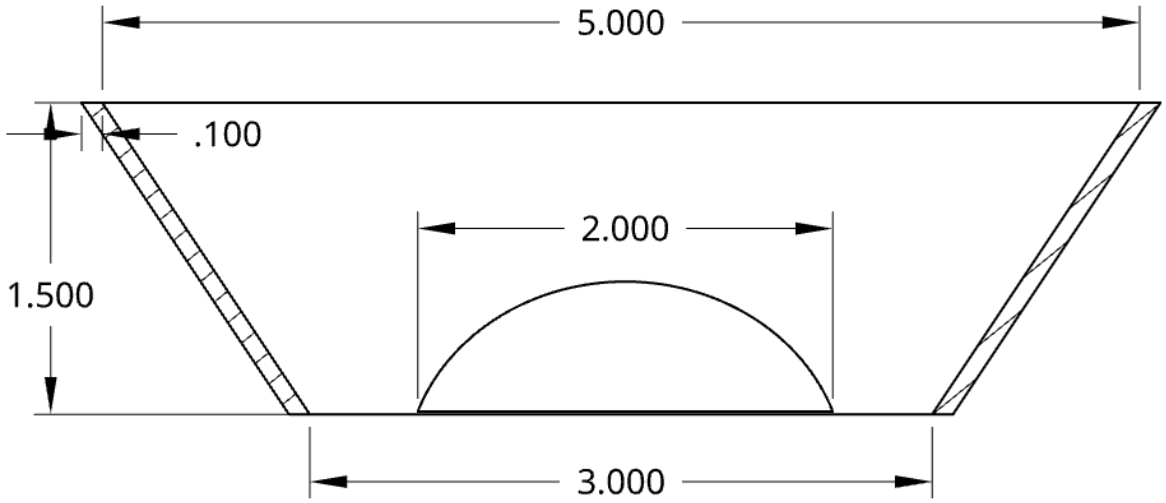

FIGURE A.3: Drawing of the simulated Conical Geometry from Ch. 5.

radial position	0^o	30^o	45^o	60^o
4 cm	5.8 kV	20.8 kV	36.8 kV	61.8 kV
4.5 cm	13 kV	22.4 kV	33.6 kV	57 kV
5 cm	16.3 kV	22.6 kV	31.1 kV	50.5 kV
5.5 cm	18.8 kV	23.1 kV	30.1 kV	44.9 kV
6 cm	28.4 kV	30.6 kV	31 kV	54.4 kV

TABLE A.4: Cutoff voltages for Argon I ions entering the Conical Geometry

A.4 Wave Configuration

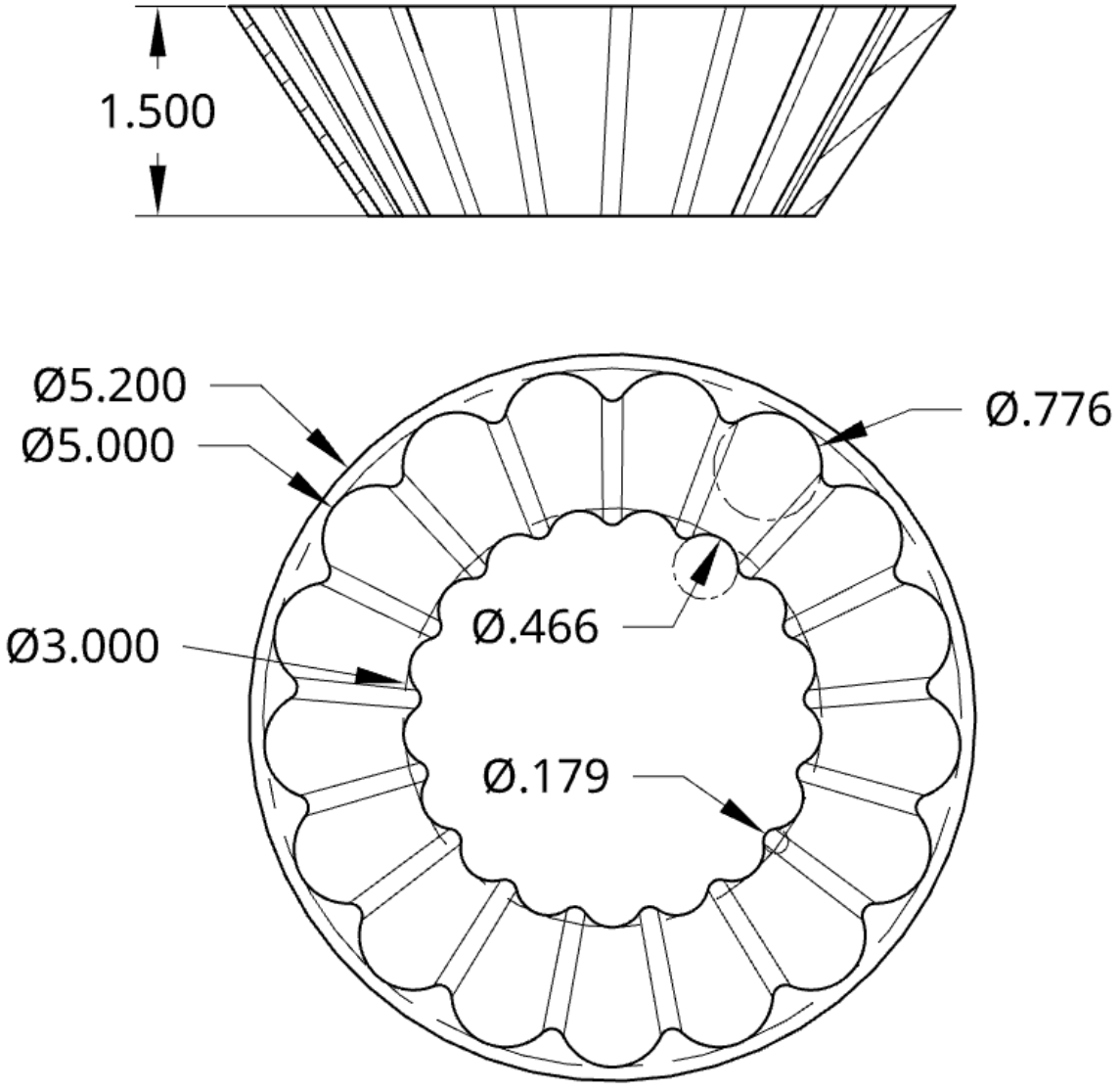

FIGURE A.4: Drawing of the simulated Wave Geometry from Ch. 5. Negative collector omitted, but identical to Fig. A.3.

radial position	0^o	30^o	45^o	60^o
4 cm	5.5 kV	20.8 kV	36.8 kV	63.6 kV
4.5 cm	13.2 kV	23 kV	34.3 kV	53.4 kV
5 cm	16.5 kV	22.7 kV	30.5 kV	53.4 kV
5.5 cm	19.6 kV	36.8 kV	54.8 kV	51.7 kV
6 cm	37.7 kV	61.5 kV	232 kV	322 kV

TABLE A.5: Cutoff voltages for Argon I ions entering the Wave Geometry, aligned with a valley region

radial position	0^o	30^o	45^o	60^o
4 cm	10 kV	22.2 kV	36.7 kV	59.3 kV
4.5 cm	14.2 kV	21.8 kV	34.9 kV	58.3 kV
5 cm	16.6 kV	24.7 kV	31.8 kV	50.5 kV
5.5 cm	49.8 kV	23.8 kV	38.8 kV	62.5 kV

TABLE A.6: Cutoff voltages for Argon I ions entering the Wave Geometry, aligned with an edge region. The edge extends beyond the 6 cm point.

Appendix B

Example Scripts

Script for calculating the normalized electric potential between collector surfaces.

```
%% Script to calculate the normalized electric potential between two ...
    surfaces of arbitrary shape.
%John Correy, University of Washington
close all
clear all
clc

% zmax ≠ 0.06

%% Import Geometry Files
% Requires files in compadible format for Cathode, Anode, and the space in
% between. Program will calculate potential on the space object, with the
% others for display purposes only.
model = createpde(3);
importGeometry(model,'Test_Geometry_Space.stl'); %Imports the space ...
    file geometry as the PDE model
cathode = importGeometry('Test_Geometry_Cathode.stl'); %Imports the ...
    cathode object
anode = importGeometry('Test_Geometry_Anode.stl'); %Imports the anode ...
    object
```

```
17
18 %% Determine Face Numbers
19 %This section only relevant during setup, to determine how MATLAB has
20 %labeled the faces
21 %figure
22 %pdegplot(model,'FaceLabels','on','FaceAlpha',0.2) % creates simple 3D ...
       model
23 %axis equal
24
25 %% Assign conditions
26 %Recommended to keep at 1 and 0 and scale later. The calculation then
27 %represents normalized voltage
28 V_Cath = 1; %Voltage at cathode-contacting surfaces
29 V_An = 0; %Voltage at anode-contacting surfaces
30 applyBoundaryCondition(model,'mixed','Face',[1:5],...
31                              'u',[0,0],'EquationIndex',[1,2],...
32                              'q',[0;0;0],'g',[0;0;0]); % establish full ...
                                   space with everything values at zero
33 applyBoundaryCondition(model,'dirichlet','Face',4,'u',[V_Cath;V_Cath;V_Cath]); ...
       % modify boundary for cathode
34 applyBoundaryCondition(model,'dirichlet','Face',[1,2],'u',[V_An;V_An;V_An]); ...
       % modify boundary for anode
35 generateMesh(model);
36 figure
37 pdeplot3D(model)
38 f = [0;0;0]; % source charge (constant)
39 CA = specifyCoefficients(model,'m',0,...
40                               'd',0,...
41                               'c',1,...
42                               'a',0,...
43                               'f', f); % specify Poisson's equation
44 potential = solvepde(model);
```

```
45 V = potential.NodalSolution; % extract potential values from PDE results
46 pdeplot3D(model,'ColorMapData',V(:,3), 'FaceAlpha', 0.5) % Plot potential
47 colormap jet
48 hold on
49 pdegplot(cathode) % show cathode
50 hold on
51 pdegplot(anode) % show anode
52 hold on
53
54 %% Convert data to more useful formats
55 coords = model.Mesh.Nodes; % Separate points into independent X, Y, and ...
       Z arrays
56 X = coords(1,:);
57 Y = coords(2,:);
58 Z = coords(3,:);
59 %figure
60 %plot3(coords(1,:),coords(2,:),coords(3,:),'o') %Ensure X, Y, and Z ...
       outputs are alligned
61 EX = potential.XGradients(:,1)'; % Extract electric potential in ...
       cartesian vectors from scalar potential function
62 EY = potential.YGradients(:,1)';
63 EZ = potential.ZGradients(:,1)';
64
65 %% Plot useful results
66 interval = 25; % Sampling interval for electric potential points. ...
       Speeds up processing
67 %quiver3(X(1:interval:end),Y(1:interval:end),Z(1:interval:end),EX(1:interval:end),EY(1:i
       %
68 %[xx,yy,zz] = meshgrid(min(X):max(X),min(Y):max(Y),min(Z):max(Z))
69 iInt = .001; %set interpolation interval in meters
```

```
70 [xx,yy,zz] = meshgrid(round(min(X),3)-iInt:iInt:round(max(X),3)+iInt, ...
       round(min(Y),3)-iInt:iInt:round(max(Y),3)+iInt, ...
       round(min(Z),3)-iInt:iInt:round(max(Z),3)+iInt); % create meshgrid ...
       of useable points
71 VInterp = interpolateSolution(potential,xx,yy,zz,[1]); % interpolate ...
       PDE results over meshgrid
72 VInterp = reshape(VInterp,size(xx)); % Reshape interpolated results for ...
       easier use
73 figure
74 contourslice(xx,yy,zz,VInterp,0,[],[],1000) % Plot cross section of the ...
       potential
75 colormap jet
76 axis equal
77 axis off
78 view(90,0)
```

Script for calculating the path of particles traveling through the field determined by the previous script.

```
1  %% NOT INDEPENDENT!! RUN AFTER RELEVANT GEOMETRY HAS BEEN CALCULATED
2  %% Script to propagate a particle through a non-uniform electric field
3  %John Correy, University of Washington
4
5  %% Voltage and Field Scaling
6  % Set the maximum voltage separation. This will correct the normalization
7  % from the potential calculations
8  Vmax = 10000; % sets the maximum voltage
9  VInterpScaled = VInterp*Vmax; %scales the interpolated potentials
10
11 [EXInterp, EYInterp, EZInterp] = gradient(VInterpScaled); % calculate ...
       the electric field from the interpolated potential
```

```
EXInterp = -1.*EXInterp;
EYInterp = -1.*EYInterp;
EZInterp = -1.*EZInterp;

B = [0,0,0]; %magnetic field, T

%% Set up figures
figure
pdeplot3D(model,'ColorMapData',V(:,3)*Vmax, 'FaceAlpha', 0.5)
hold on
pdegplot(cathode, 'EdgeLabels','off')
hold on
pdegplot(anode, 'EdgeLabels','off')
hold on
%figure
%quiver3(xx,yy,zz,EXInterp,EYInterp,EZInterp)
% figure
% contourslice(xx,yy,zz,VInterpScaled,0,[],[],1000)
% colormap jet
% axis equal
% axis off
% xlabel('x (meters)')
% view(90,0)

hold on
zMax = 0.06; %maximum value of geometry, set manually
zMin = -0.01; %maximum value of geometry, set manually

%% Establish particle parameters and starting trajectories
q = 1.6021*10^-19; %define particle charge
m = 40*1.672*10^-27; %define particle mass
r = [0,0.05,0.065;
```

```
44        %0,0.05,0.04;
45        %0,0.05,0.04;
46        ]; %define starting positions, m
47  v = [%6.35*10^3,0, -11*10^3;
48        %11*10^3,0, -11*10^3;
49        %19*10^3,0, -11*10^3;
50        0, 0, -11*10^3]; %define starting velocities, m/s
51
52  %% Propagate particles
53  dt = 10^-7; % define timestep, seconds
54  for k = 1:1:length(r(:,1)) % Simulate each particle in the array
55      for t = 0:dt:(dt*100) %simulate a given particles through the fields
56          dvEx = q/m*interp3(xx,yy,zz,EXInterp,r(k,1),r(k,2),r(k,3)); % ...
                calculate the effect of the electric field in the X direction
57          dvEy = q/m*interp3(xx,yy,zz,EYInterp,r(k,1),r(k,2),r(k,3)); % ...
                calculate the effect of the electric field in the Y direction
58          dvEz = q/m*interp3(xx,yy,zz,EZInterp,r(k,1),r(k,2),r(k,3)); % ...
                calculate the effect of the electric field in the Z direction
59          dvM = q/m*cross(v(k,:),B); % calculate the effect of the ...
                magnetic field
60          plot3(r(k,1),r(k,2),r(k,3),'k.')
61          if (r(k,3) < zMax)
62              if (isnan(dvEx) == 1)
63                  if (isnan(dvEy) == 1)
64                      break % abort propagation if particle collides with ...
                            walls
65                  end
66              end
67          end
68          if (r(k,3) < zMin)
69              break % abort propagation
70          end
```

```
71          dvEx(isnan(dvEx)) = 0; % protect from interpolation errors
72          dvEy(isnan(dvEy)) = 0;
73          dvEz(isnan(dvEz)) = 0;
74          dvx = dvEx+dvM(1);
75          dvy = dvEy+dvM(2);
76          dvz = dvEz+dvM(3);
77          v(k,1) = v(k,1)+dvx*dt; %propagate speed
78          v(k,2) = v(k,2)+dvy*dt;
79          v(k,3) = v(k,3)+dvz*dt;
80          r(k,1) = r(k,1)+v(k,1)*dt; %propagate position
81          r(k,2) = r(k,2)+v(k,2)*dt;
82          r(k,3) = r(k,3)+v(k,3)*dt;
83          %pause(0.001) % delay full plots
84      end
85  end
```

Bibliography

[1] Joseph A Angelo, *Encyclopedia of space and astronomy*. Facts on File, 2006, p. 293.

[2] Joseph J. Schlesak, Adrian Alden, and Tom Ohno, "A Microwave Powered High Altitude Platform," May 1988.

[3] Guy Pignolet, "Antenna Designs for Wireless Power Transportation: The Grand Bassin Case Study in Réunion Island," 1996.

[4] Biao Hu, Hao Li, Tianming Li, Haiyang Wang, Yihong Zhou, Xiaoyun Zhao, Xin Hu, Xuekun Du, Yulong Zhao, Xiang Li, Tian Qi, Mohamed Helaoui, Wenhua Chen, and Fadhel Ghannouchi, "A long-distance high-power microwave wireless power transmission system based on asymmetrical resonant magnetron and cyclotron-wave rectifier," *Energy Reports*, 2020.

[5] M. F. Salbani, M. A. Abdul Halim, A. H. Jahidin, and M. S. A. Megat Ali, "Helical Antenna Design for Wireless Power Transmission: A Preliminary Study," Jun. 2011.

[6] NASA, "Past Projects: Beamed Power Research," Aug. 2009, [Online]: `https://www.nasa.gov/centers/dryden/history/pastprojects/Beam/index.html` (visited on 05/25/2021).

[7] Jordin T. Kare, Fred Mitlitsky, and Andrew Weisberg, "Preliminary Demonstration of Power Beaming With NonCoherent Laser Diode Arrays," 1999.

[8] Hiroshi Matsumoto, "Research on Solar Power Satellites and Microwave Power Transmission in Japan," *IEEE Microwave Magazine*, Dec. 2002.

[9] Geoffrey A. Landis, "Applications for Space Power by Laser Transmission," May 1994.

[10] Timothy Ziemba, "Experimental Investigation of the Mini-Magnetospheric Plasma Propulsion Prototype," PhD dissertation, University of Washington, 2003.

[11] Ian Johnson, "Expanding the Capabilities of the Pulsed Plasma Thruster for In-Space and Atmospheric Operation," PhD dissertation, University of Washington, 2015.

[12] James Robert Prager, "Experimental Investigation of Plasma Downstream of a High Power Helicon," PhD dissertation, University of Washington, 2008.

[13] R. Winglee, T. Ziemba, L. Giersch, J. Prager, J. Carscadden, and B. R. Roberson, "Simulation and laboratory validation of magnetic nozzle effects for the high power helicon thruster," *Physics of Plasmas*, Vol. 14, No. 6, Jun. 2007.

[14] B. Race Roberson, "Experimental Investigation into the Enhanced Diamagnetic Perturbations and Electric Currents Downstream of the High Power Helicon Plasma Thruster," PhD dissertation, University of Washington, 2013.

[15] Nao Murakami, "High-Power Helicon Double Gun Thruster," Master's thesis, University of Washington, 2017.

[16] Keon Vereen, "Investigation of a Cluster of High-Power Helicon Thrusters for Advanced In-Space Electric Propulsion Applications," PhD dissertation, University of Washington, 2019.

[17] "High Power Helicon Thruster," [Online]: `http://earthweb.ess.washington.edu/space-propulsion/heliconthruster.php`.

[18] Leonard D. Cassady, Benjamin W. Longmier, Chris S. Olsen, Maxwell G. Ballenger, Greg E. McCaskill, Andrew V. Ilin, Mark D. Carter, Time W. Glover, Jared P. Squire, and Franklin R. Chang Diaz, "VASIMR Performance Results," Jul. 2010.

[19] Jared P. Squire, Mark D. Carter, Franklin R. Chang Diaz, Matthew Giambusso, Andrew V. Ilin, and Christopher S. Olsen, "Development Toward a Spaceflight Capable VASIMR® Engine and SEP Applications," Aug. 2014.

[20] T. Lafleur, C. Charles, and R. W. Boswell, "Ion beam formation in a very low magnetic field expanding helicon discharge," *Physics of Plasmas*, No. 4, 2010.

[21] D Gary Swanson, *Plasma Waves, 2nd Edition*. IOP Publishing Ltd, 2003.

[22] Dwight R Nicholson, *Introduction to plasma theory*. 1983.

[23] Francis F. Chen, "Plasma ionization by helicon waves," *Plasma Physics and Controlled Fusion*, Vol. 33, No. 4, 1991.

[24] Max Light and Francis F. Chen, "Helicon wave excitation with helical antennas," *Physics of Plasmas*, Vol. 2, No. 4, Apr. 1995.

[25] Francis F. Chen, "Physics of helicon discharges," *Physics of Plasmas*, Vol. 3, No. 5, Jan. 1996.

[26] Christian M. Frank, Olaf Grulke, and Thomas Klinger, "Physics of helicon discharges," *Physics of Plasmas*, Vol. 10, No. 1, Jan. 2003.

[27] Saikat Chakraborty Thakur, Christian Brandt, Lang Cui, Jordan James Gosselin, and George R. Tynan, "Formation of the Blue Core in Argon Helicon Plasma," *IEEE Transactions on Plasma Science*, Vol. 43, No. 8, Aug. 2015.

[28] F F Chen Max Light and P L Colestock, "Quiescent and unstable regimes of a helicon plasma," *Plasma Sources Science and Technology*, Vol. 11, No. 3, Jun. 2002.

[29] H. M. Mott-Smith and Irving Langmuir, "The Theory of Collectors in Gaseous Discharges," *Physical Review*, Vol. 28, Oct. 1926.

[30] Edward P. Szuszczewicz, "Area Influences and Floating Potentials in Langmuir Probe Measurements," *Journal of Applied Physics*, Vol. 43, No. 3, 1972.

[31] M. Tajmar, "Electric Propulsion Plasma Simulations and Influence on Spacecraft Charging," *Journal of Spacecraft and Rockets*, Vol. 39, No. 6, Dec. 2002.

[32] R. J. Goldston and P. H. Rutherford, *Introduction to Plasma Physics*. Taylor Francis Group, LLC, 1995.

[33] R. Udiljack, D. Anderson, M. Lisak, V. E. Semenov, and J Puech, "Improved model for multipactor in low pressure gas," *Physics of Plasmas*, Vol. 11, No. 11, 2004.

[34] Paige E. Northway, Chayse A. Aubuchon, Hunter P. Mellema, Robert M. Winglee, and Ian K. Johnson, "Pulsed Plasma Thruster Gains in Specific Thrust for CubeSat Propulsion," Jul. 2017.